



Radiosonde observations of environments supporting deep moist convection initiation during RELAMPAGO-CACTI

T. Connor Nelson*

*Department of Atmospheric and Oceanic Sciences, University of Colorado Boulder, Boulder,
Colorado*

James Marquis

Pacific Northwest National Laboratory, Richland, Washington[†]

Adam Varble

Pacific Northwest National Laboratory, Richland, Washington

Katja Friedrich

*Department of Atmospheric and Oceanic Sciences, University of Colorado Boulder, Boulder,
Colorado*

**Corresponding author address:* T. Connor Nelson, Department of Atmospheric and Oceanic Sciences, University of Colorado Boulder, 311 UCB, Boulder, Colorado 80309

E-mail: Timothy.Nelson-1@colorado.edu

[†]Additional affiliation: Department of Atmospheric and Oceanic Sciences, University of Colorado Boulder, Boulder, Colorado

Early Online Release: This preliminary version has been accepted for publication in *Monthly Weather Review*, may be fully cited, and has been assigned DOI 10.1175/MWR-D-20-0148.1. The final typeset copyedited article will replace the EOR at the above DOI when it is published.

ABSTRACT

The Remote Sensing of Electrification, Lightning, and Mesoscale/Microscale Processes with Adaptive Ground Observations (RELAMPAGO) and Cloud, Aerosol, and Complex Terrain Interactions (CACTI) projects deployed a high-spatiotemporal-resolution radiosonde network to examine environments supporting deep convection in the complex terrain of central Argentina. This study aims to characterize atmospheric profiles most representative of the near-cloud environment (in time and space) to identify the mesoscale ingredients affecting storm initiation and growth. Spatiotemporal autocorrelation analysis of the soundings reveals that there is considerable environmental heterogeneity, with boundary layer thermodynamic and kinematic fields becoming statistically uncorrelated on scales of 1–2 hr and 30 km. Using this as guidance, we examine a variety of environmental parameters derived from soundings collected within close proximity (30 km and 30 min in space and time) of 44 events over 9 days where the atmosphere either: 1) supported the initiation of sustained precipitating convection, 2) yielded weak and short-lived precipitating convection, or 3) produced no precipitating convection in disagreement with numerical forecasts from convection-allowing models (i.e., Null events). There are large statistical differences between the Null event environments and those supporting any convective precipitation. Null event profiles contained larger convective available potential energy, but had low free tropospheric relative humidity, higher freezing levels, and evidence of limited horizontal convergence near the terrain at low levels that likely suppressed deep convective growth. We also present evidence from the radiosonde and satellite measurements that flow-terrain interactions may yield gravity wave activity that affects CI outcome.

1. Introduction

Incorrect forecasts of the specific timing and location of the initiation of deep moist convection in operational models are a major factor limiting the predictability of severe weather, hydrology, and accuracy of quantitative precipitation forecasting (e.g., Davis et al. 2003; Weisman et al. 2008; Duda and Gallus 2013). Operational predictability of deep moist convection initiation (hereafter, ‘CI’) is limited by a number of factors, including our ability to routinely sample environments supporting it with adequate spatial and temporal resolution, as well as an incomplete understanding of environment-cloud interactions supporting growing congestus (e.g., Crook 1996; Weckwerth and Parsons 2006; Houston and Niyogi 2007; Lock and Houston 2014; Rousseau-Rizzi et al. 2017; Weckwerth et al. 2019). For CI to occur, the atmosphere requires three fundamental ingredients: static instability, moisture, and a triggering mechanism (e.g., surface air mass boundaries, orographic circulations, gravity waves, mesoscale convergence associated with low-level jets) to facilitate the local convergence of moisture below cloud base, deepen the boundary layer, lift and reduce layers of static stability, and to vertically accelerate parcels to their levels of free convection (*LFC*) such that they can sustainably release convective available potential energy (*CAPE*) (e.g., Weckwerth and Parsons 2006; Wilson and Roberts 2006; Weckwerth et al. 2019). Even then, parcels that do reach their LFCs may not yield CI due to entrainment of surrounding dry air (e.g., Zhao and Austin 2005; Damiani et al. 2006; Markowski et al. 2006) or other suppressing effects, such as encountering vertical wind shear (e.g., Peters et al. 2019). Atmospheric soundings are heavily relied upon to measure the potential of an environment to yield CI owing to their simultaneous characterization of vertical profiles of moisture, static instability, and wind shear (e.g., Mueller et al. 1993; Ziegler and Rasmussen 1998). A recent example by Lock and Houston (2014)(hereafter LH14) examined a number of sounding parameters from operational model

analyses during a two-year climatology of observed initiating and non-initiating deep convective storms on the U.S. Great Plains. Although a variety of environments were hospitable to CI, they found that the ingredient commonly differentiating initiating versus non-initiating convection was related to the strength of lift present in the background environment (both aloft and associated with surface boundaries), followed by the vertical excursion required for a parcel to reach its *LFC*, *CAPE*, and convective inhibition (*CIN*).

Given uncertainties often associated with simulated environments and physical parameterizations, a variety of field campaigns, such as the Convection Initiation and Downdraft Experiment (Wilson et al. 1988), International H2O Project (Weckwerth et al. 2004), Convective and Orographically-induced Precipitation Study (Wulfmeyer et al. 2008), Cumulus Photogrammetry Insitu and Doppler Observations (Damiani et al. 2008), the first and second Verification of the Origins of Rotation in Tornadoes Experiments (Rasmussen et al. 1994; Wurman et al. 2012), Mesoscale Predictability Experiment (Weisman et al. 2015), and Plains Elevated Convection at Night (Geerts et al. 2017) projects have sought to observe convective environments with targeted radiosonde launches deployed at finer spatiotemporal resolution than is capable by the U.S. operational National Weather Service radiosonde network (horizontal spacing ~ 300 km). Studies using data from these and other sources have illustrated significant environmental variability surrounding focal areas of CI owing to: intersections between air masses (e.g., Wilson and Mueller 1993; Kingsmill 1995; Ziegler and Rasmussen 1998; Markowski et al. 2006; Arnott et al. 2006; Buban et al. 2007; Wakimoto and Murphey 2009), complex terrain (e.g., Banta and Schaaf 1987; Tucker and Crook 2005; Hagen et al. 2018; Kirshbaum et al. 2018), and convective boundary layer circulations occurring on the meso-gamma-scale (e.g., Wilson et al. 1992; Wilson and Mueller 1993; Atkins et al. 1995; Weckwerth et al. 1996; Fabry 2006). Based on such studies, a routine operational profiling network is likely to under-represent variability of environments supporting

convection, yielding poor model forecasts (Romine et al. 2016; Kerr et al. 2017; Degelia et al. 2019). More likely, an array of radiosondes with horizontal spacing resolving at least $O[10\text{-km}]$ features is necessary to adequately characterize environmental heterogeneity associated with CI events (Brooks et al. 2001; Fabry 2006; Markowski and Richardson 2007; Parker 2014).

Several studies have indicated that some of the deepest and potentially most intense convection in the world initiates and develops near the Andes Mountains and smaller proximal terrain features located in Argentina (e.g., Zipser et al. 2006; Romatschke and Houze Jr. 2010; Houze Jr. et al. 2015). Motivated by these findings, the Remote Sensing of Electrification, Lightning, and Mesoscale/Microscale Processes with Adaptive Ground Observations (RELAMPAGO; Nesbitt et al. 2016) and Cloud, Aerosol, and Complex Terrain Interactions (CACTI; Varble et al. 2019) projects took place during the 2018–2019 warm convective season near Córdoba, Argentina. These projects deployed a diverse set of mobile and fixed-site instrumentation to observe interactions between the mesoscale environment and the local topography that yield: the initiation of deep moist convection, subsequent severe weather episodes, upscale growth of storms, hail processes, and cloud electrification. Among this instrumentation was a network of portable balloon radiosonde facilities, typically launching hourly from up to six sites within a $\sim 80\text{ km} \times 80\text{ km}$ area to characterize mesoscale heterogeneity of the convective boundary layer and free troposphere immediately surrounding deep moist convection. This high-resolution network had the important benefit of often yielding vertical profiles of the near-cloud environment during CI events.

This study examines data from the unprecedentedly high-resolution radiosonde network deployed during RELAMPAGO-CACTI to characterize differences in sounding-derived atmospheric conditions deemed best representative of the near-cloud environment on days in which CI occurs and days when it does not despite being forecasted by convective-allowing numerical models. To accomplish this goal, we perform an autocorrelation analysis on data collected from the high-

resolution radiosonde array, which guides our definition of a near-cloud environment profile in the context of the surrounding meso-beta-scale environmental spatiotemporal heterogeneity. Section 2 briefly outlines the data utilized during this analysis, section 3 characterizes the spatiotemporal analysis used to determine the near-cloud environment in the context of the surrounding mesoscale heterogeneity, and section 4 analyzes profiles deemed best representative of the near-cloud environment of successful and unsuccessful CI events. Summary and conclusions are presented in section 5.

2. Data overview

An ensemble of Weather Research and Forecasting (WRF) convection-allowing numerical models (CAMs), employing 3–4-km horizontal grid spacing, were run by various institutions participating in the project, including the Colorado State University (CSU) and the University of Illinois Urbana-Champaign (UI). Based on this guidance, a suite of mobile instruments was deployed within intensive observing domains near the Sierras de Córdoba (SDC) mountain range (~2880 m ASL maximum peak elevation) in the Córdoba province of central Argentina, as well as in the Mendoza province near the Andes mountains (Fig. 1; Rasmussen and Houze Jr 2016). The primary mobile observational suite included three mobile X-band Doppler on Wheels radars (Wurman et al. 1997) and six mobile balloon radiosonde platforms (Schumacher 2019; Center for Severe Weather Research 2019). For missions occurring in the Córdoba province, mobile instrumentation was deployed in coordination with fixed-site instruments provided by the U.S. Department of Energy (DOE) Atmospheric Radiation Measurement (ARM) program, including two fixed radiosonde sites (launching at variable frequency between 3–12 hr; (Holdridge et al. 2018)) and a scanning C-band precipitation radar (Bharadwaj et al. 2018). Specifications for each radiosonde system employed is provided in Table 1.

There were seven observing missions during the joint RELAMPAGO-CACTI project period (November–December 2018) dedicated to characterizing mesoscale environments and processes associated with CI events using the full array of available mobile and fixed resources (2, 6, 21, 26, and 29 November; 4 and 16 December; Fig. 1, Table 2). In addition to observations collected during the seven CI-focused missions, radiosondes launched during two missions with a severe weather focus that happened to sample the near-cloud environment at the time of CI were included in our analyses (one sounding from 10 November and one from 25 November; Fig. 1).

The array of six mobile radiosonde teams was deployed with a typical horizontal spacing of 15–45 km, performing synchronized hourly launches during 6–8-hr periods. Radiosondes launched from the DOE-ARM site every three hours between 12–00 UTC were included in the analysis when CI missions occurred in the vicinity. The 1-Hz sounding data were quality-controlled by a variety of measures, including: automated flagging, standard in ‘Level-1’ data processing using NCAR’s ASPEN software package (<https://www.eol.ucar.edu/software/aspn>); visual inspection and exclusion from analysis for obvious data signal issues (e.g., GPS errors, descending balloon rates, or large amounts of missing data); and low-pass filtering using a nine-point forward-backward binomial smoother on standard variables (e.g., temperature, dew point temperature, and wind). Additional binomial filtering was applied to sounding-derived parameter profiles (such as vertical velocity; discussed further in section 4) to smooth unresolvable noise. Based on uncertainty of their accuracy, shallow surface superadiabatic layers were reduced or eliminated by excluding data concurrent with measured lapse rates exceeding $25^{\circ}\text{C km}^{-1}$. Due to the disparity in launch elevation across the complex terrain (0.4–1.6 km above mean sea level; hereafter ASL), we perform a vertical height coordinate transformation following Gal-Chen and Somerville (1975) and Parker (2014) that preserves data altitude above ground level (hereafter AGL) at low-levels (e.g., below 700-hPa) and height ASL aloft. This transformation allows for direct comparisons of

soundings launched at different altitudes and compositing of soundings across a common vertical reference frame.

3. Defining the near-cloud environment

The primary goal of this study is to identify and differentiate key near-cloud environmental conditions supporting or suppressing CI. To do so, we first determine the capabilities of the radiosonde network to adequately represent the near-cloud environment by employing a sounding autocorrelation analysis similar to Nelson et al. (2020). Correlations between neighboring and consecutive vertical profiles of potential temperature (θ), vapor mixing ratio, horizontal wind, lapse rate of θ , and vertical wind shear inform upon the spatial and temporal scales of environmental heterogeneity observed across the radiosonde network during each CI mission. Prior to performing this analysis, each sounding is interpolated to a uniform 50-m vertical data spacing and the mean vertical profile of each variable assumed representative of the atmospheric base state ($\bar{\chi}$) is subtracted from each individual sounding, yielding an array of detrended data (χ'). Analysis of the detrended data reduces artificially large autocorrelations due to similar base states (Janert 2011; Nelson et al. 2020). For the spatial autocorrelation analysis, correlation coefficients ($C_{\chi',dist}$) are computed from the detrended profiles,

$$C_{\chi',dist}(i, j) = \text{Corr}(\chi'_i, \chi'_j), \quad (1)$$

where i and j are indices representing arbitrarily-paired soundings from all radiosondes contemporaneously launched within an hour of when the first CI episode occurred (or was forecasted to occur if it did not in reality) on each day. We iterate i and j from 1– n (where n is the total number of contemporaneous soundings) until a unique $C_{\chi',dist}$ is calculated for all paired launch sites. Cor-

relograms of $C_{\chi',dist}$ are plotted as a function of the mean horizontal distance (d) between paired soundings along their vertical flight paths (z),

$$d(i, j) = \sqrt{(x_i(z) - x_j(z))^2 + (y_i(z) - y_j(z))^2}, \quad (2)$$

and are averaged over all CI missions (Fig. 2a, b).

For the temporal analysis, correlation coefficients ($C_{\chi',time}$) are computed between all hourly consecutive detrended soundings launched from an instrument site on each day,

$$C_{\chi',\tau}(i, t) = \text{Corr}(\chi'_{i,t}, \chi'_{i,\tau}) \quad (3)$$

and

$$\tau = t + \delta t, \quad (4)$$

where t is the sounding launch time closest to the first CI episode at one launch site (denoted by the index i) and δt is a positive or negative hourly launch interval relative to t . This calculation is conducted iteratively over all sounding sites (from $i=1$ to n). Thus, there are unique temporal autocorrelation values and times for each sounding pair (t, τ) at each sounding site i . Correlograms are plotted as a function of τ , and averaged across each sounding site and all days (Fig. 2c, d).

We perform the autocorrelation analysis separately within the boundary layer (defined in section 4) and the free troposphere owing to the variety of synoptic, mesoscale, and diurnal mechanisms that can affect their evolution¹. Critical spatial and temporal scales to best represent the near-cloud environment in our cases (i.e., the length-scales smaller than those quantifying significant local

¹Only data collected below 9.0 km are considered because the sounding network most consistently measured below this altitude. Soundings from the 10 and 25 November cases were not included in this analysis because the radiosonde array was deployed to sample environments supporting specific severe weather events rather than mesoscale variability supporting CI.

mesoscale heterogeneity) are estimated by detecting when neighboring profiles become effectively uncorrelated (e.g., at the 0.5-autocorrelation level; Nelson et al. 2020).

Within the free troposphere, neighboring profiles are effectively spatially uncorrelated at horizontal distances between 20–80 km, depending on the atmospheric variable considered. For example, neighboring θ profiles decorrelate at relatively large distances (> 70 km; Fig. 2b); whereas, the lapse rate of θ decorrelates at smaller length scales (< 20 km). However, spatial autocorrelations for neighboring profiles within the boundary layer decorrelate at considerably shorter length scales (< 30 km; Fig. 2a), particularly for the kinematic variables (Fig. 2b). Larger variability in the boundary layer is perhaps expected when considering variable land cover, complex topography across the region, and generally smaller scales of circulations controlling the kinematic and thermodynamic properties at low levels.

Consecutively-launched soundings generally are temporally-uncorrelated between 1–4 hr both prior to and after CI within the free troposphere (Fig. 2d). For any given variable, boundary layer profiles tend to evolve on slightly faster time scales (~ 1 hr) than in the free troposphere (Fig. 2c). The exceptions to this are vapor mixing ratio profiles, which are correlated over longer time scales at low levels than in the free troposphere (Fig. 2c, d). Examination of soundings at particular sites shows that mid-level (~ 700 – 500 -hPa) moisture increases over time, especially within the 2 hrs prior to CI time, possibly due to horizontal advection of moist air or ascending moist boundary layer thermals that lead to decorrelation in the free troposphere. The autocorrelations for certain variables (e.g., free tropospheric θ or meridional wind) suggest slower evolving profiles prior to a CI event than after it (i.e., there is a more rapid environmental evolution post-CI than pre-CI). However, the overall differences between autocorrelation time scales preceding and succeeding a CI event, or within the boundary layer and the free troposphere, are small for most variables (1–2 hr).

The autocorrelations shown in Figure 2 are averaged across all RELAMPAGO-CACTI CI-focused missions. Additional tests dividing the spatial and temporal autocorrelations between successful and unsuccessful CI attempts (discussed more in section 4) yielded no statistical difference, suggesting an overall similar magnitude of environmental heterogeneity regardless of the convective outcome. Comparisons of neighboring synchronized radiosonde soundings collected on particular days illustrate, for example, that the pre-CI water vapor mixing ratio profiles in the lower free troposphere could vary by as much as $3\text{--}5\text{ g kg}^{-1}$ over ~ 20 km distances (Fig. 3). Such variances may be partly a result of mesoscale environmental heterogeneity, but also a result of the free tropospheric moistening by detrainment of cumulus (evident by relatively moist profiles nearest to the SDC ridgeline, where congestus most typically formed; red profiles in (Fig. 3)).

These results suggest that it might be necessary to sample length scales less than 20 km in the boundary layer and 40 km in the free troposphere to unambiguously characterize ambient near-cloud surroundings in complex environments (Nelson et al. 2020). Thus, this data set echoes sentiments of past studies that raise caution over the use of appropriate proximity soundings to represent convective environments (e.g., Brooks et al. 2001; Markowski and Richardson 2007, 2010). It is important to note that some of the decorrelation scales analyzed within the boundary layer are below the native spatial resolution of the observations and, therefore, are only estimates. However, it seems reasonable to conclude that the true decorrelation scales are likely below the 30 km average sounding spacing (Nelson et al. 2020). This may be especially true when considering the spatial scales of mesoscale ascent and moisture convergence associated with many common CI triggering mechanisms (e.g., along surface boundaries and orographic circulations), which typically are smaller than 10 km (e.g., Markowski et al. 2006; Arnott et al. 2006; Stonitsch and Markowski 2007; Marquis et al. 2007; Buban et al. 2007; Barthlott et al. 2010). Such variation may not be thoroughly-represented by the RELAMPAGO-CACTI radiosonde array; therefore, use of

the soundings in this article focuses on convective metrics derived from the individual soundings that best represent the near-cloud environment. Furthermore, the atmosphere is likely evolving on temporal scales relevant to CI finer than those suggested by the 0.5-autocorrelation threshold discussed herein. For example, weakly precipitating, short-lived convective clouds commonly occurred less than 2 hr prior to the initiation of stronger and longer-lived storms, owing to steady removal of *CIN*. Therefore, although this analysis suggests that hourly sounding observations appear to be adequate for characterizing bulk evolution of the atmosphere, sub-2-hr observation frequency could be important for relatively subtly evolving convection-supporting phenomena.

4. Near-cloud environments

A variety of convective outcomes are observed across the cases considered in this study. To help identify characteristics of the environments potentially relevant to CI, we employ an approach similar to LH14, except that we use observed rather than model soundings and consider environments supporting convection of variable intensity and duration by classifying them in the following ways:

1. Initiation of Sustained Convection (“CI”): Isolated convective storms occur at the approximate time and location predicted by numerical forecasts, and they attain a maximum observed radar reflectivity echo greater than 35 dBZ (similar to Wilson and Schreiber 1986; Wilson and Roberts 2006; Lima and Wilson 2008; Rasmussen and Houze Jr 2016; Alexander et al. 2018)² for longer than 20 min, detected at low levels by the nearest radar in the RELAMPAGO-CACTI observing array.
2. Failed Convection Initiation (“Fail”): This is similar to the CI classification except that maximum observed radar reflectivity echoes near the ground do not exceed 35 dBZ for at least

²Collectively, these studies use a 30–40 dBZ threshold. We utilize 35 dBZ because the ensemble of radars used during RELAMPAGO-CACTI included variable frequencies and peak powers, with a roughly 3–6 dBZ variance for many common targets.

20 min. However, maximum reflectivity greater than light drizzle must be detected. This category is intended to differentiate CI events from those that failed to produce sustained precipitation. Often, these events occur 1–2 hr prior to successful CI events.

3. Null cases (“Null”): For two cases (21 November, 16 December) no precipitation greater than light drizzle was detected near the ground by radar within the intensive observing domain, despite forecasts by a majority of the WRF-CAM ensemble.

Hereafter, parameters of soundings that most closely represent the near-cloud environment in space and time are examined for each of these three observed event types. Guided by the results shown in section 3, soundings deemed most representative of successful CI events are those collected within 30 km and 30 min of the location and time that radar reflectivity associated with a convective cell first exceeds 35 dBZ near the ground. Soundings representing Fail environments are those launched within 30 km and 30 min of the greatest observed near-surface radar reflectivity echo (though, not exceeding 35 dBZ for more than 20 min). When consecutive hourly soundings at a launch site are collected within 30-min of an event, the earlier of the two soundings is used. The locations of the CI and Fail soundings, with respect to observed radar reflectivity and terrain is provided in Figure 4. With respect to Null events, it is tricky to precisely define an environment representative of convection that did not occur. We consider a sounding most representative of a Null environment if no precipitating convection is observed in reality, but: 1) the sounding is collected within 30 km distance of CI event forecasted by a member of the WRF-CAM ensemble (Fig. 5), and 2) it contains the maximum integrated parcel buoyancy between the ground and the *LFC* of all soundings at a given site within a two-hour window containing the forecasted CI time (i.e., when boundary layer parcels had the least *CIN* within the forecasted CI window). Forecasted CI time in such events is based on the first occurrence of simulated radar reflectivity greater

than 35 dBZ and cloud top heights above 5 km altitude in hourly model forecast output. In all events, only those occurring greater than 50 km away from existing deep convection are considered. Although this specific distance is arbitrary, it aims to isolate the impact of the background environment on new convection rather than marginally-observed processes originating from preceding mature storms. One CI event is known to occur as a result of lifting along a surface-based cold pool originating from distant convection (10 November; Fig. 4b). Soundings are manually removed from our sample if the profiles are saturated, suggesting the environment at the measurement site is already contaminated by convection. Although it is our aim to target soundings best representative of the near-cloud inflow environment in time and space, the flow directly entering cloud base may not be fully sampled by the sounding array.

The number of CI, Fail, and Null soundings on each of the nine observing days is shown in Table 2. All soundings were uniquely classified as one of the three event types. Out of 44 classified soundings, 13 were representative of CI events, 19 of Fail events, and 10 of Null events. Out of the 13 CI soundings, only one was associated with relatively short-lived (duration < 40 min) and/or weak (maximum near-surface radar reflectivity < 45 dBZ) precipitating convection, perhaps analogous to the short-duration events described by Soderholm et al. (2014). An important caveat to consider during the following sounding analysis involves the relatively small sample size (44 soundings across nine days). *Thus, the diversity of background meteorological conditions sampled in our data set is potentially limited.* Furthermore, multiple CI and Fail events took place during some missions, sometimes in close spatiotemporal proximity, yielding potential ambiguity in the subjective choice of event representativeness.

We investigate a variety of environmental parameters from these soundings. It is feasible to investigate a nearly infinite list of sounding parameters to correlate with each event type. However, to help narrow the list of parameters to ones of most physical relevance, we begin with analogs

interrogated by LH14, including: *CAPE*, *CIN*, shear and lapse rate within and below the active cloud bearing layer (hereafter, *ACBL*), and vapor mixing ratio difference between the surface and 1.5 km above LFC (*MRD*). Variables that depend upon the initial altitude of a lifted parcel (e.g., *CAPE*; *CIN*; lifting condensation level, *LCL*; *LFC*; equilibrium level, *EL*) are computed using a variety of parcel origins: 1) a surface parcel, 2) a parcel assumed to have properties equal to the mean of the lowest 100-hPa of the sounding, and 3) the most unstable parcel in the profile. As in many studies, *CAPE* (*CIN*) is defined as the total positive (negative) integrated parcel buoyancy above (below) the *LFC*³. In addition to those examined by LH14, we also consider:

1. Environmental freezing height ($Z_{T=0}$ in Table 3): It is hypothesized that lower environmental freezing levels could increase ice microphysical processes and release of the latent heat of fusion at lower depths within the cloud, increasing parcel buoyancy and more effective precipitation processes.
2. Integrated buoyancy (*IB*) and vertical distribution of *CIN*: *IB* sums both the positive and negative buoyancy of a parcel below the *LFC*, estimating the net buoyant acceleration at low levels. This value differs from *CIN* in the presence of superadiabatic layers or complex temperature inversion patterns. The cumulative depth of the layer(s) over which a parcel experiences negatively buoyant acceleration is also calculated (related to depth of initial parcel height to *LFC*, called ΔZ_s , from Houston and Niyogi (2007) and LH14).
3. Boundary layer depth (Z_{BL} in Table 3): We calculate the boundary layer depth using two methods, comparable to Sivaraman et al. (2013). One method locates the height, working upward from the surface, at which the bulk Richardson number drops below 0.5 (Sorensen et al. 1998). A second boundary layer depth is estimated by finding the height at which $\frac{d\theta}{dz}$

³*CAPE* is calculated by integrating between the *LFC* and 350-hPa, the highest common altitude across all soundings. Statistics assessing the *EL* exclude the small sample of five incomplete soundings (2 CI, 1 Fail, and 2 Null).

exceeds 0.5 K km^{-1} (Liu and Liang 2010). The final boundary layer height is taken to be the maximum of these two estimates.

4. Depth of boundary layer moisture: Computed to explore the hypothesis that boundary layer moisture, deepened by low-level convergence, increases the probability of CI (e.g., Wilson et al. 1992; Ziegler et al. 1997, 2007). We calculate the altitude at which the vapor mixing ratio drops to either 10 g kg^{-1} ($Z_{q=10}$) or 80% of the surface value ($Z_{q=0.8q(0)}$).
5. Moisture above the boundary layer: The average dew point depression above the boundary layer ($T - T_d$) and specifically within the mid-levels (600–400-hPa) is computed to quantify the dryness of the air that may be entrained into growing cumulus from within the free troposphere.
6. Lapse rate tendency: The mean tendency below 700-hPa, between 700–500-hPa, and 500–350-hPa is computed as the difference between the measured lapse rates at the time most representative of a CI, Fail, or Null event and the prior launch time. In the absence of a prior sounding, the subsequent sounding is used. These data are used to explore the hypothesis that CI occurs when $CAPE(CIN)$ is maximized(minimized).
7. Radiosonde-derived vertical motion (w): LH14 note a strong link between CI and background lift, particularly near and below the LFC . Lacking reliable direct measurements of w throughout the observing domain, we estimate it from sounding data by subtracting an ascent rate predicted by the balloon size, assumed expansion during ascent, and total package weight from the GPS-measured balloon ascent rate (Wang et al. 2009). The estimated combined radiosonde package weight is 0.24 kg and we assume a uniform drag coefficient of 0.65. A potentially significant source of error is that the observed ascent rate is sensitive to its surface fill volume, which can vary between sounding operators (even when a standard fill

amount is set)⁴. The radiosonde-derived w is believed to be accurate within $\pm 1\text{--}2\text{ m s}^{-1}$ (e.g., Wang et al. 2009). We examined alternative methods to retrieve w ; e.g., using an expression for lapse rate tendency (Markowski and Richardson 2010) or vertical integration of horizontal convergence measured by neighboring soundings (not shown). Though both methods produce similar estimates of mean error variance to the GPS-measured retrieval method, the profiles contained either significant noise or were unrealistically smooth and near zero throughout their depth compared to the more realistic GPS-measured retrieval method. Given the typical deployment of the radiosonde network, it is likely that sounding-retrieved vertical motion most commonly reflects background synoptic ascent/descent that might be expected to alter static stability and moisture that deepening clouds would encounter at remote locations from a sounding.

8. Low-level mean state variables: Mean temperature, relative humidity, static stability (Brunt–Väisälä frequency), and horizontal wind are averaged within the lowest 100-hPa of the atmosphere to explore relationships between boundary layer properties and surface-based CI.
9. Flow-terrain interaction: We estimate the Scorer parameter (l^2 ; Scorer 1949), mountain Froude number (F_n ; Mannis and Sawford 1982; Brady and Waldstreicher 2001), and mean low-level flow relative to terrain orientation to explore the interactions of the mesoscale flow and the local topography that may affect CI (e.g., Hagen et al. 2018; Kirshbaum et al. 2018). The F_n calculations do not include four of the CI soundings and two of the Fail soundings on 6 November, because they were associated with convection occurring near a smaller secondary terrain feature (the Sierras Chicas range) where cross-terrain flow was not confidently characterized by the soundings, and one on 10 November, where the relative importance of

⁴Wang et al. (2009) also note that balloon sounding-derived vertical velocity is often overestimated up to 5 km due to the combined effects of environmental vertical velocity, perturbation ascent rate associated with turbulence, and drag coefficient-Reynolds number assumptions.

the topography on the triggering of CI was ambiguous because initiation occurred along a cold pool gust front near the Sierras Chicas. For the l^2 calculations, individual profiles are computed for each sounding considered at a vertical resolution of 500-m. An additional filtering step is then applied using a second nine-point binomial filter to each median profile to reduce potentially erroneous noise due to finite difference calculations⁵.

In total, we examined 70 atmospheric parameters calculated from the ensemble of CI, Fail, and Null soundings (Table 3). For brevity, only parameters that are statistically different across the three event types (Table 4), as well as select sounding parameters typically used to assess convective environments are discussed. The means for the full list of all tested parameters across all the event types is provided as Supplementary Material.

a. Statistically-significant environmental parameters

We first explore the environmental parameters that are statistically different across the three event types by comparing them using two-sample Kolmogorov-Smirnov (K-S) tests at the 95% confidence level (Table 4). We use the K-S test because the data may not be normally distributed. The accompanying mean soundings computed across each event type at a vertical resolution of 500-m are shown in Figures 6, 7. Overall, there are few sounding metrics that *exclusively* differentiate CI from Null, including: *ML* mean ACBL lapse rate (-7.81 K km^{-1} for Null and -6.62 K km^{-1} for CI), maximum bulk wind shear (15.06 m s^{-1} for Null and 20.09 m s^{-1} for CI), *LL u* (-1.29 m s^{-1} for Null and -3.48 m s^{-1} for CI), and low-level lapse rate tendency (1.68 K km^{-1}

⁵While the additional filtering does smooth the profiles, it makes the interpretation of the profiles more robust to erroneous single data point outliers or shallow discrete layers where the horizontal wind is near zero, yielding unrealistically high values of l^2 , and smaller sample sizes for certain groups of soundings. We also note that the results of the Scorer parameter calculations are sensitive to the order in which smoothing and compositing is done, and the interpretation of the results (i.e., diagnosing trapped versus vertically propagating lee waves) is sensitive to the smoothing applied.

hr^{-1} for Null and $0.16 \text{ K km}^{-1} \text{ hr}^{-1}$ for CI)(Table 4). There are also few sounding metrics that *exclusively* differentiate Fail from Null (mean Fail environments have lower precipitable water, more negative $MU\ IB$, and higher $LCLs$) or that statistically differentiate all three environments (MRD and $MU\ MRD$, discussed further below)(Table 4). Indeed, CI and Fail soundings were quite similar, with few statistically different parameters, including the aforementioned MRD and $MU\ MRD$ (6 g kg^{-1} for Fail and 7 g kg^{-1} for CI), and $ML\ CIN$ (48.52 J kg^{-1} for Fail and 32.72 g kg^{-1} for CI), as well as some sounding-derived w parameters. The statistically significant w -derived parameters indicate that the Fail soundings, on average, have stronger background ascent than the CI soundings by $1\text{--}2 \text{ m s}^{-1}$, especially in the low-levels (Table 4, Fig. 7f). Most of the environments contain retrieved w profiles that monotonically decrease with height, which may represent the mean surrounding atmosphere (Fig. 7f). The mean Null sounding, however, has comparable ascent above 600-hPa to the mean Fail sounding (Fig. 7f). Unfortunately, the range of uncertainty associated with the radiosonde-retrieval of w generally increases with altitude, and the mean values presented are within the typical $1\text{--}2 \text{ m s}^{-1}$ error range (Fig. 7f, Nelson et al. 2019). This caveat makes it difficult to compare our results with the findings of LH14, who found lift to be important for predicting CI.

The majority of the statistical differences across the data set are between the Null soundings, and the combined population of CI and Fail soundings (“c, d” labels in Table 4). The combined CI and Fail sounding population had statistically: lower ELs , more positive mid-level lapse rate tendency (i.e., becoming increasingly unstable prior to initiation)(e.g., Fig. 7b), and weaker low-level meridional wind compared to the Null soundings (e.g., Fig. 6). As in LH14, a variety of $CAPE$ calculations statistically differentiate event types. However, in our samples, Null environments contained the largest mean surface, MU , and $ML\ CAPE$ ($\sim 800\text{--}1000 \text{ J kg}^{-1}$; Table 4, Fig. 6c). In contrast, the Fail soundings had the smallest $CAPE$ ($\sim 400 \text{ J kg}^{-1}$; Table 4, Fig. 6b). The

statistically higher *CAPE* for the Null soundings is also likely due to the statistically warmer low-level temperatures (+5 K; *LL* θ in Table 4, Fig. 6). Because of varying degrees of boundary layer and surface heating, the Null and Fail soundings are slightly less statically stable at low levels than the CI soundings, but the low levels became increasingly unstable for the CI and Null events (though, only statistically significant for the Null events below 700-hPa) (Fig. 7a, b; Table 4). The Null soundings, however, have a deeper positive (destabilizing) lapse rate tendency throughout the boundary layer (height of approximately 1.4 km and 740-hPa) (Fig. 7b). This finding may not be surprising because the CI soundings themselves may be sampling shadowed areas below developing cumulus and anvils, while the Null soundings are sampling comparatively clear skies.

Although this analysis suggests that many aspects of the Null environments might be superior for supporting growing convection, they contained higher environmental freezing levels (Table 4) than the CI and Fail cases, which is perhaps suppressive of convective growth because of delayed initiation of beneficial ice microphysical processes and additional latent heating occurring at higher altitudes. Also, despite the Null events having larger magnitudes of vapor mixing ratio extending over larger depths at low levels than the CI and Fail events ($Z_{q=10}$ and *MRD* in Table 4, Fig. 7e) and having comparable relative humidity at low levels (Fig. 7e), they contain significantly smaller free tropospheric relative humidity, with $T - T_d$ in excess of 20 °C (Table 4, Figs. 6 and 7d, e). Further, the spread of these moisture variables do not appreciably overlap between the Null and combined CI and Fail events. Thus, updrafts in the Null environments could be more prone to destructive entrainment effects aloft, especially given the relatively higher mean altitude of strongest shear in the Null environments being located within much drier free tropospheres (Figs. 6c and 7d), despite having the weakest shear overall. Although lapse rates are steepening in the Null boundary layers more so than the CI and Fail events, lapse rates for all categories are near zero, above 700-hPa, with large standard deviations that occupy a similar spread (mid-level *LRT* of -0.16 K km^{-1}

hr^{-1} in Table 4, Fig. 7b). This may be suppressive of cloud deepening overall by lessening deep layer *CAPE*; though, most of the stabilizing lapse rate tendency occurs above the typical capping inversion height (Fig. 6). In contrast, the mean CI and Fail soundings are slowly destabilizing from the surface up to 500–600-hPa, which would lead to increasing deep layer *CAPE* (Table 4, Fig. 7b).

Another potential caveat to consider in this statistical analysis involves an observational bias based on the resources available for CI missions during the project. For example, other RELAMPAGO science foci were often preferred missions on days with relatively high *CAPE* and shear. *Thus, CI environments most optimally sampled during the project may be biased toward environments with relatively low *CAPE*⁶ shear, or other convective-supportive parameters, which may impact comparisons of our data set with past literature.*

b. Non-statistically significant parameters

There were a variety of tested parameters that, perhaps surprisingly, did not prove to statistically differentiate the three event types. All soundings had their most unstable parcels originating from within the boundary layer in the lowest 450-m, suggesting that the observed convection was boundary layer driven, rather than elevated. However, the mean boundary layer depths measured across the three event types were rather similar (1.2–1.7 km). Further, although the Null events generally had the smallest *CIN* and most positive *IB* (Fig. 8), few measures of *CIN* or *IB* were statistically different among the three event types; *MU IB* was statistically more negative for the Fail cases than the Null cases and *ML CIN* was stronger for the Fail cases than the CI cases. The mean *CIN* (*IB*) generally was larger (more inhibitive) for Fail events than for CI or Null events

⁶The largest *LFC*-to-350-hPa *CAPE* for any CI case included in this analysis, ~ 1100 J/kg, was observed during a mission with a severe weather focus from a radiosonde that was opportunistically deployed near a CI location.

(Fig. 8), owing to a slightly smaller low-level mean relative humidity. The mean Null profiles have considerable spread in *ML CIN* and *IB*; however, mean values are larger (more inhibitive) for Fail events. Because Fail events usually occur a few hours prior to CI events, it is plausible that the observed decrease in *CIN* between Fail and CI events is due to factors such as steady destabilizing of the capping inversion from local mesoscale lift, moistening and cooling of the lower free troposphere from detrainment of cumulus, or deepening of the convective boundary layer. While the mean Fail environments indicate conditions that are generally less favorable for initiating and sustaining convection, *CAPE*, subcloud wind shear, *LFC* height, *IB*, and *CIN* (surface or *MU*) are not statistically different from the ensemble of CI event soundings. Thus, it is also likely that factors like entrainment or other effects that parcel theory and sounding-derived ingredient-based analysis alone cannot address are important governors of CI.

Though not significantly different, mean upper level horizontal winds, primarily westerly in all cases, are generally stronger during the CI and Fail events than during the Null events, by approximately 5 m s^{-1} (Fig. 6). Although vector mean wind speeds in the lower half of the atmosphere are weak across all event types, mean wind direction is significantly more northerly throughout low-levels during the Null events than during the CI and Fail events, which are more easterly (this is the only wind parameter that statistically-differs between the combined CI and Fail profiles and the Null profiles; *LL v* in Table 4). Thus, it might be expected that the CI and Fail events had stronger upslope flow promoting more effective mechanical lifting of parcels than in the Null events (Soderholm et al. 2014; Kirshbaum et al. 2018). Terrain-relative vector mean winds in the lowest 100-hPa of each sounding collected east of the SDC⁷ indicate that, although the Null environments have the largest terrain-parallel wind component, there is a similar mean

⁷Most of the CI events occurred along the SDC, therefore, this analysis is limited to soundings collected during missions focused near this range, specifically, on the eastern side (upstream of the peak, relative to the low-level flow, and downstream relative to the upper-level flow)

upslope wind magnitude for all event types, differing by generally less than $1\text{--}2\text{ m s}^{-1}$ (Fig. 9). Kirshbaum (2011) found, however, that even somewhat small increases in the terrain-relative wind ($O[1\text{ m s}^{-1}]$) could hamper the chances for orographic CI by disrupting or displacing the low-level convergence relative to the topographic thermal forcing. Contrary to his findings, our mean Null environments have the weakest overall terrain-perpendicular (upslope) flow of all cases, while CI cases had the strongest. Due to the similarity in the terrain-perpendicular wind, there are no statistical differences in F_n ⁸ for the CI, Fail, or Null events. Therefore, the differences in upslope flow do not appear to differentiate event types.

Various studies provide evidence suggesting that vertical wind shear may affect the deepening of cumulus by tilting updraft structure, altering adverse vertical pressure gradient forces, or modulating focus areas of entrainment of the surrounding environment into the cloud (e.g., Zhao and Austin 2005; Damiani et al. 2006; Markowski et al. 2006; Peters et al. 2019); albeit, the impact of shear on CI is not well understood. Though all of the soundings have comparable wind shear below the altitude of the maximum terrain, the mean Null environments have weaker shear within the *ACBL* ($6\text{--}8\text{ m s}^{-1}$ bulk shear) than the mean CI and Fail environments ($8\text{--}10\text{ m s}^{-1}$ bulk shear), especially in the $750\text{--}350\text{-hPa}$ layer (Fig. 7c). Thus, the mean CI (Null) soundings have the largest (weakest) wind shear overall. Interestingly, the altitudes of maximum shear, respectively, were not found to be statistically different. Regardless, given the exceptionally dry free troposphere comprising the mean Null environments (e.g., Fig. 7d), large shear ($> 5\text{ s}^{-1}$) may not have been necessary to effectively dissipate congestus via entrainment.

⁸ F_n can only be meaningfully calculated for situations where the atmosphere below the terrain height was stable (i.e., θ increases with height).

15% of the CI, 37% of the Fail, and 58% of the Null soundings have neutral or unstable layers at low levels.

c. Possible terrain factors differentiating CI, Fail, and Null events

To further understand environmental differences between Null events and the combined CI and Fail event population, we interpret the radiosonde data in the context of mesoscale conditions and possible terrain influences. Cloud top heights estimated with combined GOES-16 infrared brightness temperatures and corresponding radiosonde temperature profiles (e.g., Hamada and Nishi 2010), were relatively shallow during the Null cases (21 November and 16 December) compared to those from other CI or Fail cases (estimated 7–9 km for Null events versus 11–16 km for CI and Fail events), with only short-lived anvil clouds (if at all) and drizzle-sized or smaller hydrometers detected near the ground within the observing network. Furthermore, a prominent stationary (albeit, expanding) O[10 km]-wide clear sky region was present within the observing network near the SDC peak for both Null cases, especially on the lee side (Fig. 10), suggesting a region of localized static stability, dryness, or descent downstream (relative to the flow at middle- through upper-levels; i.e., above ~ 500 -hPa) of the ridgeline.

As mentioned above, the mean soundings (on the east side of the highest terrain of the SDC) have similar magnitudes of the upslope wind component. Approximating horizontal mass convergence as the cross-terrain differential of terrain-orthogonal flow from soundings collected on both sides of the SDC (when available), the CI and Fail cases both have a region of weak divergence extending from the height of the terrain peak up through mid-levels (Fig. 11). In contrast, the Null cases had a region of even weaker, near zero, divergence within this layer. It is ambiguous to infer convergence below the level of the terrain peak using this data; however, deeper mean convergence is implied within the boundary layer for the CI and Fail cases than for the Null cases. Thus, mean CI and Fail events contain a slightly more defined column of low-level convergence topped with mid-level divergence than the mean Null profile, implying a more significant low- to mid-level

updraft implied by mass continuity. However, there is appreciable case-to-case variability using this method, which neglects a terrain-parallel component owing to instrument limitations, some sensitivity to sounding selection (not shown), and possible underestimation of the magnitude of convergence and divergence because of the horizontal observation spacing being larger than the length scale of the terrain circulation features, each increasing uncertainty of the results.

The mean Null profile on the east (downstream, relative to mid-upper-level flow) and west (upstream, relative to mid-upper-level flow) sides of the SDC has a more pronounced temperature inversion above the boundary layer (Fig. 12a), and a stronger component of the terrain-crossing wind up to 500-hPa than the western mean profile for the other event types (Fig. 12e). These environmental mean differences relative to the orography motivate us to examine evidence that convective outcome may be influenced by terrain-flow interactions.

The upstream (west of the SDC) Scorer parameter and F_n both up- and downstream of the topography (west and east of the SDC, respectively), demonstrate measures of the flow traversing the terrain and the potential for terrain-induced gravity waves (e.g., Brady and Waldstreicher 2001; Sachsperger et al. 2015)(Figs. 12, 13). Mean F_n values west of the SDC were less than 0.02 for both the Null and combined CI and Fail sounding populations, but east of the terrain were 0.18 and 0.14, respectively. As a result, sub-critical, strongly-blocked upslope flow on the lee side is suggested in all event types, with CI events alone having the least blocked flow ($F_n = 0.34$). It should be noted that the simplistic F_n calculation implies that all of the upward forcing is due to the terrain, wind, and environmental stability alone. In reality, there may be a complex mix of mechanically- and thermally-driven mesoscale updraft forcing mechanisms, which the F_n analysis alone cannot dissect.

While there is a considerably strong inversion on the western side of the terrain between 750–650-hPa during the Null cases, there is not a collocated supercritical peak in the mean Scorer

parameter profile. Rather, there is a steep decrease of the Scorer parameter with height from the surface up to 500-hPa. The lack of a supercritical zone in the area of the strong inversion could be due to smoothing of the raw Scorer parameter profiles in the mean. In principle, however, a large decrease of the Scorer parameter above a supercritical zone, or a region of high l^2 , indicates conditions that may be favorable for trapped lee waves (Durrán and Klemp 1982; Brady and Waldstreicher 2001; Sachsperger et al. 2015). The mean combined CI and Fail profile contains a comparatively gentle decrease in the Scorer parameter with height on the west side of the terrain, suggesting conditions supportive of comparatively lower amplitude trapped or vertically propagating lee waves, if any at all (Durrán and Klemp 1982; Brady and Waldstreicher 2001; Sachsperger et al. 2015). Thus, there is at least some indirect evidence from the sounding data set that flow interactions with the terrain may partly differentiate mesoscale processes associated with the occurrence of CI.

5. Summary

In this study, we evaluated near-cloud environments supporting or suppressing the initiation of deep moist convection measured by the high-resolution radiosonde array (hourly launches from six sites, spaced ~ 30 km apart) deployed during the RELAMPAGO and CACTI field campaigns. To most objectively characterize the near-cloud environment using the sounding array, we performed a spatiotemporal autocorrelation analysis across geographically-neighboring and consecutive hourly radiosonde launches. This analysis indicated that there was appreciable variance in the sounding data within the boundary layer, where spatially- and temporally-neighboring profiles are generally uncorrelated within 1–2 hr and < 30 km distance from any given radiosonde launch. Within the free troposphere, these sampling limits were more forgiving (2–3 hr and ~ 50 km). These findings support a variety of studies urging caution when characterizing a convective

environment using a sounding representative of a location and time offset by $> O(10 \text{ km})$ and $> 1 \text{ hr}$ (e.g., Brooks et al. 2001; Fabry 2006; Markowski and Richardson 2007; Parker 2014). Our autocorrelation methodology, along with an in-depth analysis of other high-quality observations from the data set, could provide the opportunity for future work to more accurately quantify the meso-beta-scale heterogeneity of convective environments surrounding the complex terrain of the region.

Using our sounding autocorrelation analysis as guidance for spatiotemporal criteria necessary to sample the near-cloud environment, we examined environments sampled by radiosondes collected within 30 km and 30 min of: 1) the initiation of sustained precipitating convection (“CI” events), 2) the generation of weak and short-lived transient precipitating convection (“Fail” events), and 3) events with no detected precipitating convection despite being forecasted by CAMs (“Null” events). Assessing 44 soundings collected over eight days, we found that there were only a few environmental parameters that statistically differentiated CI and Fail environments. Namely, Fail events had smaller differences between near-surface and free tropospheric moisture and more MU CIN than the CI events. Despite the overall lack of statistical difference between Fail and CI events, the results suggest that a plausible difference between them is the subtle erosion of CIN over time, eventually leading to successful CI over the course of a few hours.

Null environments were the most statistically different among the three event types. They contained larger mean $CAPE$ ($\sim 800\text{--}1000 \text{ J kg}^{-1}$), higher ELs ($\sim 12 \text{ km}$), and warmer surface and boundary layers ($d\theta \sim +5 \text{ K}$) than CI or Fail events. Parcels lifted from Null profiles did not contain statistically larger CIN or more negative IB , except for mixed-layer parcels. Scorer parameter profiles suggest indirect evidence that mountain wave activity due to flow interactions with the terrain may also differentiate Null events. Null environments contained statistically much lower relative humidity throughout the free troposphere and higher freezing levels than their CI or Fail

counterparts. Thus, effects not commonly accounted for in parcel theory assumptions, such as entrainment of dry free tropospheric air into the developing updraft or delayed production of ice and release of latent heat of fusion likely contributed to the Null outcomes. The entrainment effect may be particularly important to consider in the context of our current work, because the model forecasts used to define our Null events employed horizontal grid spacings of 3–4 km. Recent studies suggest that simulations with a grid spacing of this size may produce excessively wide updrafts that may be unrealistically immune to dilution by entrainment (e.g., Varble et al. 2014, 2020; Bryan and Morrison 2012; Lebo and Morrison 2015; Morrison 2017), potentially yielding erroneous CI forecasts.

The results of this study are encouraging and important for discerning environmental parameters likely directly impacting the observed precipitating convection, or lack thereof, during the RELAMPAGO-CACTI CI missions. Though incorrect model forecasts of CI were inherent to the definition of a Null event, it was beyond the current scope of our study to present a complete analysis of model shortcomings. Our analysis allows for the discernment of important observed near-cloud environmental profiles supporting or suppressing CI, and motivates a thorough investigation into model performance for a variety of outcomes. It should also be noted that the depth, intensity, and persistence of mesoscale updraft regions, and thermodynamic modifications to the environment directly within them, are important details to fully understand CI processes. This study does not directly address such details because they are unlikely to have been consistently measured by the radiosonde array. The authors are currently pursuing efforts to integrate these sounding analyses with three-dimensional radar observations of specific RELAMPAGO-CACTI CI missions to examine details of the triggering mechanisms, and cloud-scale large eddy simulation using composite mean soundings from the three event types to explore important updraft-environment interactions. Such analyses will allow further direct comparisons to other convection

and CI-focused modeling studies (e.g., Houston and Niyogi 2007; Kirshbaum 2011, 2013; Madaus and Hakim 2017; Rousseau-Rizzi et al. 2017).

Acknowledgments. This work is funded by NSF grant AGS-1661707 and by the U.S. Dept. of Energy's of Science Biological and Environmental Research as part of the Atmospheric System Research program. Pacific Northwest National Laboratory is operated by Battelle for the U.S. Department of Energy. Data utilized are available on NCAR's Earth Observing Laboratory and Atmospheric Radiation Measurement Data Discovery catalogs. Sounding analysis and plots were partly generated using MetPy. This work benefited from helpful discussions with Matt Parker, Steve Nesbitt, Karen Kosiba, Russ Schumacher, Paul Robinson Jeff Trapp, Lynn McMurdie, Jim Wilson, Robert Wallace, and Nicholas Luchetti. We would like to thank three anonymous reviewers, and all RELAMPAGO-CACTI organizers and field participants.

References

- Alexander, L. S., D. M. Sills, and P. A. Taylor, 2018: Initiation of convective storms at low-level mesoscale boundaries in southwestern Ontario. *Wea. Forecasting*, **33**, 583–596, doi:10.1175/WAF-D-17-0086.1.
- Arnott, N. R., Y. P. Richardson, J. M. Wurman, and E. M. Rasmussen, 2006: Relationship between a weakening cold front, misocyclones, and cloud development on 10 June 2002 during IHOP. *Mon. Wea. Rev.*, **134**, 311–335, doi:10.1175/MWR3065.1.
- Atkins, N. T., R. M. Wakimoto, and T. M. Weckwerth, 1995: Observations of the sea-breeze front during CaPE. Part II: Dual-Doppler and aircraft analysis. *Mon. Wea. Rev.*, **123**, 944–969.
- Banta, R., and C. B. Schaaf, 1987: Thunderstorm genesis zones in the Colorado Rocky Mountains as determined by traceback of geosynchronous satellite images. *Mon. Wea. Rev.*, **115**, 463–476.

- Barthlott, C., J. W. Schipper, N. Kalthoff, B. Adler, C. Kottmeier, A. Blyth, and S. Mobbs, 2010: Model representation of boundary-layer convergence triggering deep convection over complex terrain: A case study from COPS. *Atmos. Res.*, **95**, 172–185, doi:10.1016/j.atmosres.2009.09.010.
- Bharadwaj, N., J. Hardin, B. Isom, I. Lindenmaier, A. Matthews, and D. Nelson, 2018: C-Band Scanning ARM Precipitation Radar (CSAPR2CFRPPI). Atmospheric Radiation Measurement (ARM) user facility, September 23, 2018. Accessed 1 Sept 2019, doi:10.5439/1482633.
- Brady, R., and J. Waldstreicher, 2001: Observations of mountain wave-induced precipitation shadows over northeast Pennsylvania. *Wea. Forecasting*, **16**, 2810–300.
- Brooks, H. E., C. A. Doswell III, and J. Cooper, 2001: On the environments of tornadic and nontornadic mesocyclones. *Wea. Forecasting*, **9**, 606–618.
- Bryan, G. H., and H. Morrison, 2012: Sensitivity of a simulated squall line to horizontal resolution and parameterization of microphysics. *Mon. Wea. Rev.*, **140** (1), 202–225, doi:10.1175/MWR-D-11-00046.1.
- Buban, M. S., C. L. Ziegler, E. N. Rasmussen, and Y. P. Richardson, 2007: The dryline on 22 May 2002 during IHOP: Ground radar and in situ data analyses of the dryline and boundary layer evolution. *Mon. Wea. Rev.*, **135**, 2473–2505, doi:10.1175/MWR3453.1.
- Center for Severe Weather Research, 2019: CSWR RELAMPAGO Dataset, Version 1.0. CSWR, Accessed 24 March 2020.
- Crook, N. A., 1996: Sensitivity of moist convection forced by boundary layer processes to low-level thermodynamic fields. *Mon. Wea. Rev.*, **124**, 1767–1785.

- Damiani, R., G. Vali, and S. Haimov, 2006: The structure of thermals in cumulus from airborne dual-doppler radar observations. *J. Atmos. Sci.*, **63**, 1432–1450, doi:10.1175/JAS3701.1.
- Damiani, R., and Coauthors, 2008: The Cumulus, Photogrammetric, In Situ, and Doppler Observations experiment of 2006. *Bull. Amer. Meteor. Soc.*, **89**, 57–73, doi:10.1175/BAMS-89-1-57.
- Davis, C. A., K. W. Manning, R. E. Carbone, S. B. Trier, and J. D. Tuttle, 2003: Coherence of warm-season continental rainfall in numerical weather prediction models. *Mon. Wea. Rev.*, **131**, 2667–2679.
- Degelia, S. K., X. Wang, and D. Stensrud, 2019: An evaluation of the impact of assimilating AERI retrievals, kinematic profilers, rawinsondes, and surface observations on a forecast of a nocturnal convection initiation event during the PECAN field campaign. *Mon. Wea. Rev.*, **147**, 2739–2764, doi:10.1175/MWR-D-18-0423.1.
- Duda, J. D., and W. A. Gallus, 2013: The impact of large-scale forcing on skill of simulated convective initiation and upscale evolution with convection-allowing grid spacings in the WRF. *Wea. Forecasting*, **28**, 994–1018, doi:10.1175/WAF-D-13-00005.1.
- Durran, D. R., and J. B. Klemp, 1982: The effects of moisture on trapped mountain lee waves. *J. Atmos. Sci.*, **39**, 2490–2506.
- Fabry, F., 2006: The spatial variability of moisture in the boundary layer and its effect on convection initiation: Project-long characterization. *Mon. Wea. Rev.*, **134**, 79–91, doi:10.1175/MWR3055.1.
- Gal-Chen, T., and R. Somerville, 1975: On the use of a coordinate transformation for the solution of the Navier-Stokes equations. *J. Comput. Phys.*, **18**, 209–228, doi:10.1175/BAMS-D-15-00257.1.

- Geerts, B., and Coauthors, 2017: The 2015 Plains Elevated Convection at Night field project. *Bull. Amer. Meteor. Soc.*, **98**, 767–786, doi:10.1175/BAMS-D-15-00257.1.
- GRAW, 2020: Radiosondes DFM-09. GRAW Radiosondes, Accessed 1 Sept 2020, <https://www.graw.de/products/radiosondes/dfm-09/>.
- Hagen, M., J. v. Baelen, and E. Richard, 2018: Influence of the wind profile on the initiation of convection in mountainous terrain. *Quart. J. Roy. Meteor. Soc.*, **137**, 224–235, doi:10.1002/qj.784.
- Hamada, A., and N. Nishi, 2010: Development of a cloud-top height estimation method by geostationary satellite split-window measurement trained with CloudSat data. *J. Appl. Meteor. Climatol.*, **49**, 2035–2049, doi:10.1175/2010JAMC2287.1.
- Holdridge, D., J. Kyrouac, and E. Keeler, 2018: Balloon-Borne Sounding System (SONDEWNP). Atmospheric Radiation Measurement (ARM) user facility, September 27, 2018. Accessed 1 Sept 2019, doi:10.5439/1482633.
- Houston, A. L., and D. Niyogi, 2007: The sensitivity of convective initiation to the lapse rate of the active cloud-bearing layer. *Mon. Wea. Rev.*, **135**, 3013–3032, doi:10.1175/MWR3449.1.
- Houze Jr., R. A., K. L. Rasmussen, M. D. Zuluaga, and S. R. Brodzik, 2015: The variable nature of convection in the tropics and subtropics: A legacy of 16 years of the Tropical Rainfall Measuring Mission satellite. *Rev. Geophys.*, **53**, 994–1021, doi:10.1002/2015RG000488.
- Janert, P. K., 2011: *Data Analysis with Open Source Tools*. O'Reilly, 509 pp.
- Kerr, C. A., D. J. Stensrud, and X. Wang, 2017: Verification of convection-allowing model ensemble analyses of near-storm environments using MPEX upsonde observations. *Mon. Wea. Rev.*, **145**, 857–875, doi:10.1175/MWR-D-16-0287.1.

- Kingsmill, D. E., 1995: Convection initiation associated with a sea-breeze front, a gust front, and their collision. *Mon. Wea. Rev.*, **123**, 2913–2933.
- Kirshbaum, D. J., 2011: Cloud-resolving simulations of deep convection over a heated mountain. *J. Atmos. Sci.*, **68**, 361–378, doi:10.1175/2010JAS3642.1.
- Kirshbaum, D. J., 2013: On thermally forced circulations over heated terrain. *J. Atmos. Sci.*, **70**, 1690–1709.
- Kirshbaum, D. J., B. Adler, N. Kalthoff, C. Barthlott, and S. Serafin, 2018: Moist orographic convection: Physical mechanisms and links to surface-exchange processes. *Atmosphere*, **9**, 80, doi:10.3390/atmos9030080.
- Lebo, Z. J., and H. Morrison, 2015: Effects of horizontal and vertical grid spacing on mixing in simulated squall lines and implications for convective strength and structure. *Mon. Wea. Rev.*, **143** (11), 4355–4375, doi:10.1175/MWR-D-15-0154.1.
- Lima, M. A., and J. W. Wilson, 2008: Convective storm initiation in a moist tropical environment. *Mon. Wea. Rev.*, **136**, 1847–1864, doi:10.1175/2007MWR2279.1.
- Liu, S., and X. Liang, 2010: Observed diurnal cycle climatology of planetary boundary layer height. *J. Climate*, **23**, 5790–5809, doi:10.1175/2010JCLI3552.1.
- Lock, N. A., and A. L. Houston, 2014: Empirical examination of the factors regulating thunderstorm initiation. *Mon. Wea. Rev.*, **142**, 240–258, doi:10.1175/MWR-D-13-00082.1.
- Madaus, L. E., and G. J. Hakim, 2017: Constraining ensemble forecasts of discrete convective initiation with surface observations. *Mon. Wea. Rev.*, **145**, 2597–2610, doi:10.1175/MWR-D-16-0395.1.

- Mannis, P. C., and B. L. Sawford, 1982: Mesoscale observations of upstream blocking. *Quart. J. Roy. Meteor. Soc.*, **108**, 427–434.
- Markowski, P., and Y. Richardson, 2007: Observations of vertical wind shear heterogeneity in convective boundary layers. *Mon. Wea. Rev.*, **135**, 843–861, doi:10.1175/MWR3334.1.
- Markowski, P., and Y. Richardson, 2010: *Mesoscale meteorology in Midlatitudes*. Wiley-Blackwell, 407 pp.
- Markowski, P. M., C. Hannon, and E. Rasmussen, 2006: Observations of convection initiation “failure” from the 12 June 2002 IHOP deployment. *Mon. Wea. Rev.*, **134**, 375–405, doi:10.1175/MWR3059.1.
- Marquis, J. N., Y. P. Richardson, and J. M. Wurman, 2007: Kinematic observations of mesocyclones along boundaries during IHOP. *Mon. Wea. Rev.*, **135** (5), 1749–1768, doi:10.1175/MWR3367.1.
- Morrison, H., 2017: An analytic description of the structure and evolution of growing deep cumulus updrafts. *J. Atmos. Sci.*, **74** (3), 809–834, doi:10.1175/JAS-D-16-0234.1.
- Mueller, C. K., J. W. Wilson, and N. A. Crook, 1993: The utility of sounding and mesonet data to nowcast thunderstorm initiation. *Wea. Forecasting*, **8**, 132–146.
- Nelson, T. C., L. C. Harrison, and K. L. Corbosiero, 2019: Examination of the eXpendable Digital Dropsonde-derived vertical velocities from the Tropical Cyclone Intensity (TCI) experiment. *Mon. Wea. Rev.*, **147**, 2367–2386, doi:10.1175/MWR-D-18-0414.1.
- Nelson, T. C., L. C. Harrison, and K. L. Corbosiero, 2020: Temporal and spatial autocorrelations from expendable digital dropsondes (XDDs). *J. Atmos. Oceanic Technol.*, **37** (3), 381–399, doi:10.1175/JTECH-D-19-0032.1.

- Nesbitt, S. W., and Coauthors, 2016: RELAMPAGO experimental design overview. *EOL Catalog*, 59 pp.
- Parker, M. D., 2014: Composite VORTEX2 supercell environments from near-storm soundings. *Mon. Wea. Rev.*, **142**, 508–529, doi:10.1175/MWR-D-13-00167.1.
- Peters, J. M., W. Hannah, and H. Morrison, 2019: The Influence of Vertical Wind Shear on Moist Thermals. *J. Atmos. Sci.*, **76** (6), 1645–1659, doi:10.1175/JAS-D-18-0296.1.
- Rasmussen, E. N., J. M. Straka, R. Davies-Jones, C. A. Doswell III, F. H. Carr, M. D. Eilts, and D. R. MacGorman, 1994: Verification of the Origins of Rotation in Tornadoes Experiment: VORTEX. *Bull. Amer. Meteor. Soc.*, **75**, 995–1006.
- Rasmussen, K. L., and R. A. Houze Jr, 2016: Convective initiation near the Andes in subtropical South America. *Mon. Wea. Rev.*, **144**, 2351–2374, doi:10.1175/MWR-D-15-0058.1.
- Romatschke, U., and R. A. Houze Jr., 2010: Extreme summer convection in South America. *J. Climate*, **23**, 3761–3791, doi:10.1175/2010JCLI3465.1.
- Romine, G. S., C. S. Schwartz, R. D. Torn, and M. L. Weisman, 2016: Impact of assimilating dropsonde observations from MPEX on ensemble forecasts of severe weather events. *Mon. Wea. Rev.*, **144**, 3799–3823, doi:10.1175/MWR-D-15-0407.1.
- Rousseau-Rizzi, R., D. J. Kirshbaum, and M. K. Yau, 2017: Initiation of deep convection over an idealized mesoscale convergence line. *J. Atmos. Sci.*, **74**, 835–853, doi:10.1175/JAS-D-16-0221.1.
- Sachsperger, J., S. Serafin, and V. V. Grubišić, 2015: Lee waves on the boundary-layer inversion and their dependence on free-atmospheric stability. *J. Atmos. Sci.*, **3**, 70, doi:10.3389/feart.2015.00070.

- Schumacher, R., 2019: CSU Mobile Radiosonde Data. Version 1.0. UCAR/NCAR–Earth Observing Laboratory, Accessed 1 Sept 2019, <https://doi.org/10.26023/3QGG-JQKS-AF0G>.
- Scorer, R. S., 1949: Theory of waves in the lee of mountains. *Quart. J. Roy. Meteor. Soc.*, **75**, 41–56, doi:10.1002/qj.49707532308.
- Sivaraman, C., S. McFarlane, E. Chapman, M. Jensen, T. Toto, S. Liu, and M. Fischer, 2013: Planetary boundary layer (PBL) height value added product (VAP): Radiosonde retrievals. *DOE/SC-ARM/TR-132*, 68 pp., URL https://www.arm.gov/publications/tech_reports/doe-sc-arm-tr-132.pdf.
- Soderholm, B., B. Ronalds, and D. J. Kirshbaum, 2014: The evolution of convective storms initiated by an isolated mountain ridge. *Mon. Wea. Rev.*, **142**, 1430–1451, doi:10.1175/MWR-D-13-00280.1.
- Sorensen, J. H., A. Rasmussen, T. Ellermann, and E. Lyck, 1998: Mesoscale influence on long-range transport—evidence from ETEX modeling and observations. *Atmos. Envi.*, **32**, 4207–4217.
- Stonitsch, J. R., and P. M. Markowski, 2007: Unusually long duration, multiple-Doppler radar observations of a front in a convective boundary layer. *Mon. Wea. Rev.*, **135** (1), 93–117, doi:10.1175/MWR3261.1.
- Tucker, D. F., and N. A. Crook, 2005: Flow over heated terrain. Part II: Generation of convective precipitation. *Mon. Wea. Rev.*, **133**, 2565–2582, doi:10.1175/MWR2965.1.
- Vaisala, 2020: Radiosonde RS41. Vaisala, Accessed 1 Sept 2020, <https://www.vaisala.com/en/products/instruments-sensors-and-other-measurement-devices/soundings-products/rs41>.
- Varble, A., H. Morrison, and E. Zipser, 2020: Effects of under-resolved convective dynamics on the evolution of a squall line. *Mon. Wea. Rev.*, 289–311, doi:10.1175/MWR-D-19-0187.1.

- Varble, A., and Coauthors, 2014: Evaluation of cloud-resolving and limited area model inter-comparison simulations using TWP-ICE observations: 1. Deep convective updraft properties. *J. Geophys. Res. Atmos.*, **119**, 13 891–13 918, doi:10.1002/2013JD021371.
- Varble, A., and Coauthors, 2019: Cloud, Aerosol, and Complex Terrain Interactions (CACTI) field campaign report. *DOE/SC-ARM-19-028*, 31 pp., URL <https://www.arm.gov/publications/programdocs/doe-sc-arm-19-028.pdf>.
- Wakimoto, R. M., and H. V. Murphey, 2009: Analysis of a dryline during IHOP: Implications for convection initiation. *Mon. Wea. Rev.*, **137**, 912–936, doi:10.1175/2008MWR2584.1.
- Wang, J., J. Bian, W. O. Brown, H. Cole, and V. Grubišić, 2009: Vertical air motion from T-REX radiosonde and dropsonde data. *J. Atmos. Oceanic Technol.*, **26**, 928—942, doi:10.1175/2008JTECH3.1240.1.
- Weckwerth, T. M., J. Hanesiak, J. W. Wilson, S. B. Trier, S. K. Degelia, W. A. Gallus, R. D. Roberts, and X. Wang, 2019: Nocturnal convection initiation during PECAN 2015. *Bull. Amer. Meteor. Soc.*, **100**, 2223–2239, doi:10.1175/BAMS-D-18-0299.1.
- Weckwerth, T. M., and D. B. Parsons, 2006: A review of convection initiation and motivation for IHOP 2002. *Mon. Wea. Rev.*, **134**, 5–22, doi:10.1175/MWR3067.1.
- Weckwerth, T. M., J. W. Wilson, and R. M. Wakimoto, 1996: Thermodynamic variability within the convective boundary layer due to horizontal convective rolls. *Mon. Wea. Rev.*, **124**, 769–784.
- Weckwerth, T. M., and Coauthors, 2004: An overview of the International H2O Project (IHOP 2002) and some preliminary highlights. *Bull. Amer. Meteor. Soc.*, **85**, 253–277, doi:10.1175/BAMS-85-2-253.

- Weisman, M. L., C. Davis, W. Wang, K. W. Manning, and J. B. Klemp, 2008: Experiences with 0–36-h explicit convective forecasts with the WRF-ARW model. *Wea. Forecasting*, **23**, 407–437, doi:10.1175/2007WAF2007005.1.
- Weisman, M. L., and Coauthors, 2015: The Mesoscale Predictability Experiment (MPEX). *Bull. Amer. Meteor. Soc.*, **96**, 2127–2149, doi:10.1175/BAMS-D-13-00281.1.
- Wilson, J. W., G. B. Foote, N. A. Crook, J. C. Fankhauser, C. G. Wade, J. D. Tuttle, C. K. Mueller, and S. K. Krueger, 1992: The role of boundary-layer convergence zones and horizontal rolls in the initiation of thunderstorms: A case study. *Mon. Wea. Rev.*, **120**, 1785–1815.
- Wilson, J. W., J. A. Moore, G. B. Foote, B. Martner, A. R. Rodi, T. Uttal, and J. M. Wilczak, 1988: Convection Initiation and Downburst Experiment (CINDE). *Bull. Amer. Meteor. Soc.*, **69**, 1328–1347.
- Wilson, J. W., and C. K. Mueller, 1993: Nowcasts of thunderstorm initiation and evolution. *Wea. Forecasting*, **8**, 113–131.
- Wilson, J. W., and R. D. Roberts, 2006: Summary of convective storm initiation and evolution during IHOP: Observational and modeling perspective. *Mon. Wea. Rev.*, **134**, 23–47, doi:10.1175/MWR3069.1.
- Wilson, J. W., and W. E. Schreiber, 1986: Initiation of convective storms at radar-observed boundary-layer convergence lines. *Mon. Wea. Rev.*, **114**, 2516–2536.
- Wulfmeyer, V., and Coauthors, 2008: The convective and orographically induced precipitation study: A research and development project of the World Weather Research Program for improving quantitative precipitation forecasting in low-mountain regions. *Bull. Amer. Meteor. Soc.*, **89**, 1477–1486.

- Wurman, J., D. Dowell, Y. Richardson, P. Markowski, E. Rasmussen, D. Burgess, L. Wicker, and H. B. Bluestein, 2012: The second Verification of the Origins of Rotation in Tornadoes Experiment: VORTEX2. *Bull. Amer. Meteor. Soc.*, **93**, 1147–1170, doi:10.1175/BAMS-D-11-00010.1.
- Wurman, J., J. Straka, E. Rasmussen, M. Randall, and A. Zahrai, 1997: Design and deployment of a portable, pencil-beam, pulsed, 3-cm Doppler radar. *J. Atmos. Oceanic Technol.*, **14**, 1502–1512.
- Zhao, M., and P. H. Austin, 2005: Life cycle of numerically simulated shallow cumulus clouds. Part II: Mixing dynamics. *J. Atmos. Sci.*, **62**, 1291–1310, doi:10.1175/JAS3415.1.
- Ziegler, C. L., T. Lee, and R. A. Pielke Sr., 1997: Convective initiation at the dryline: A modeling study. *Mon. Wea. Rev.*, **125**, 1001–1026.
- Ziegler, C. L., and E. N. Rasmussen, 1998: The initiation of moist convection at the dryline: Forecasting issues from a case study perspective. *Wea. Forecasting*, **13**, 1106–1131.
- Ziegler, C. L., E. N. Rasmussen, M. S. Buban, Y. P. Richardson, L. J. Miller, and R. M. Rabin, 2007: The “triple point” on 24 May 2002 during IHOP. Part II: Ground-radar and in situ boundary layer analysis of cumulus development and convection initiation. *Mon. Wea. Rev.*, **135**, 2443–2472, doi:10.1175/MWR3411.1.
- Zipser, E. J., D. J. Cecil, C. Liu, S. W. Nesbitt, and D. P. Yorty, 2006: Where are the most intense thunderstorms on earth? *Bull. Amer. Meteor. Soc.*, **87**, 1057–1072, doi:10.1175/BAMS-87-8-1057.

LIST OF TABLES

Table 1.	Sounding types and specifications launched by the six mobile sounding teams (CSWR1, CSWR2, CSWR3, UI1, UI2, and CSU) and by the fixed DOE-ARM site (CACTI). All soundings collected data at 1-Hz and have various proprietary on-board data calibrations and error corrections (e.g., surface calibrations, telemetry error correction, hysteresis, or data packet/signal quality control measures). Specifications for the GRAW DFM-09 were obtained from GRAW (2020). Specifications for the Vaisala RS41-SG and RS41-SGP were obtained from Vaisala (2020). Also included is the total number of soundings launched on all CI missions, regardless of classification, and the two soundings obtained from 10 November and 25 November.	41
Table 2.	The number of CI, Fail, and Null soundings on each of the nine observing days and in total. The time range in UTC for each sounding type is provided for each day. Days with only one time listed had soundings only taken at that hour included as opposed to a range of hours.	42
Table 3.	Matrix of all 70 variables considered in this study, classified as ‘thermodynamic’, ‘kinematic’, or ‘composite’. * = computed from a surface, mixed-layer (lowest 100-hPa), and most unstable parcel. ** = computed from an average of the lowest 100-hPa. In this table, <i>BS</i> is bulk shear, <i>SWS</i> is bulk subcloud wind shear, <i>dV</i> is horizontal wind shear, <i>H_w</i> is the height of maximum <i>w</i> , <i>H_{LFC}</i> is the ratio of <i>H_w</i> to the <i>LFC</i> height, and <i>PW</i> is precipitable water. References inspiring examination of variables are also provided. The following abbreviations for references are used in this table only: Hagen et al. (2018) is H18, Houston and Niyogi (2007) is HN07, Kirshbaum (2011) is K11, Madaus and Hakim (2017) is MH17, Markowski and Richardson (2010) is MR10, Zhao and Austin (2005) is ZA05, and Ziegler et al. (2007) is Z07.	43
Table 4.	Subset of statistically significant (SS) sounding parameters and their abbreviations analyzed in this study. The means for the parameters representative of CI, Fail, and Null events are provided. b = statistical significance between CI and Fail, c = statistical significance between CI and Null, and d = statistical significance between Null and Fail.	44

TABLE 1. Sounding types and specifications launched by the six mobile sounding teams (CSWR1, CSWR2, CSWR3, UI1, UI2, and CSU) and by the fixed DOE-ARM site (CACTI). All soundings collected data at 1-Hz and have various proprietary on-board data calibrations and error corrections (e.g., surface calibrations, telemetry error correction, hysteresis, or data packet/signal quality control measures). Specifications for the GRAW DFM-09 were obtained from GRAW (2020). Specifications for the Vaisala RS41-SG and RS41-SGP were obtained from Vaisala (2020). Also included is the total number of soundings launched on all CI missions, regardless of classification, and the two soundings obtained from 10 November and 25 November.

Sounding teams	CSWR1–CSWR3	UI1–UI2	CSU	CACTI
Sonde type	GRAW DFM-09	GRAW DFM-09	Vaisala RS41-SG	Vaisala RS41-SGP
Pressure range	10–1100 hPa	10–1100 hPa	3–sfc hPa	3–sfc hPa
Pressure accuracy	0.5 hPa	0.5 hPa	0.04–1 hPa	0.04–1 hPa
Pressure resolution	0.1 hPa	0.1 hPa	0.01 hPa	0.01 hPa
Temperature range	–95 to 50°C	–95 to 50°C	–95 to 60°C	–95 to 60°C
Temperature accuracy	0.2°C	0.2°C	0.1–0.4°C	0.1–0.4°C
Temperature resolution	0.01°C	0.01°C	0.01°C	0.01°C
Relative humidity range	0–100%	0–100%	0–100%	0–100%
Relative humidity accuracy	4%	4%	2–4%	2–4%
Relative humidity resolution	1%	1%	0.1%	0.1%
Wind speed range	—	—	0–180 m s ^{–1}	0–180 m s ^{–1}
Wind speed accuracy	0.2 m s ^{–1}	0.2 m s ^{–1}	0.15 m s ^{–1}	0.15 m s ^{–1}
Wind speed resolution	—	—	0.1 m s ^{–1}	0.1 m s ^{–1}
Wind direction range	0–360°	0–360°	0–360°	0–360°
Wind direction accuracy	—	—	2°	2°
Wind direction resolution	—	—	0.1°	0.1°
Total number of soundings	28	36	95	73

TABLE 2. The number of CI, Fail, and Null soundings on each of the nine observing days and in total. The time range in UTC for each sounding type is provided for each day. Days with only one time listed had soundings only taken at that hour included as opposed to a range of hours.

Date	CI (time)	Fail (time)	Null (time)
2-Nov	0	0	0
6-Nov	6 (15–16 UTC)	5 (15–17 UTC)	0
10-Nov	1 (19 UTC)	0	0
21-Nov	0	0	7 (16–19 UTC)
25-Nov	1 (17 UTC)	0	0
26-Nov	1 (16 UTC)	6 (15–17 UTC)	1 (16 UTC)
29-Nov	3 (17 UTC)	3 (16 UTC)	0
4-Dec	1 (16 UTC)	5 (16–17 UTC)	0
16-Dec	0	0	4 (19–20 UTC)
Total	13	19	12

TABLE 3. Matrix of all 70 variables considered in this study, classified as ‘thermodynamic’, ‘kinematic’, or ‘composite’. * = computed from a surface, mixed-layer (lowest 100-hPa), and most unstable parcel. ** = computed from an average of the lowest 100-hPa. In this table, *BS* is bulk shear, *SWS* is bulk subcloud wind shear, *dV* is horizontal wind shear, H_w is the height of maximum *w*, H_{LFC} is the ratio of H_w to the *LFC* height, and *PW* is precipitable water. References inspiring examination of variables are also provided. The following abbreviations for references are used in this table only: Hagen et al. (2018) is H18, Houston and Niyogi (2007) is HN07, Kirshbaum (2011) is K11, Madaus and Hakim (2017) is MH17, Markowski and Richardson (2010) is MR10, Zhao and Austin (2005) is ZA05, and Ziegler et al. (2007) is Z07.

	Variable names	References
Thermodynamic	$CAPE^*$, CIN^* , LCL^* , LFC^* , EL^*	various (e.g., MR10),
	IB^* , MRD^* , $CAPE$ (within 2 km of the <i>LFC</i>) [*] , <i>ACBL</i> lapse rate [*] ,	various (e.g., MR10), LH14, LH14, LH14,
	Lapse rate tendency (<i>sfc</i> –700-hPa, 700–500-hPa, 500–350-hPa),	MR10,
	$Z_{T=0}$, $T - T_d$ (600–400-hPa, >3.5 km),	—, K11,
	$Z_{q=10}$, $Z_{q=0.8q(0)}$, static stability ^{**} , relative humidity ^{**} , θ^{**}	Z07, Z07, —, Z07, —
Kinematic	w (<i>sfc</i> to <i>LFC</i>) [*] , w (above <i>LFC</i>) [*] , BS_{ACBL}^* ,	LH14, LH14, LH14,
	SWS^* , dV_{max} , $Z(dV_{max})$, w_{max} ,	LH14, ZA05, ZA05, LH14,
	H_w , <i>BS</i> , w^{**} , u^{**} , v^{**}	LH14, ZA05, LH14, H18, H18
Composite	H_{LFC}^* , ΔZ_s , depth of CIN^* , <i>PW</i> , F_n , Z_{BL}	LH14, LH14, HN07, K11, H18, —

TABLE 4. Subset of statistically significant (SS) sounding parameters and their abbreviations analyzed in this study. The means for the parameters representative of CI, Fail, and Null events are provided. b = statistical significance between CI and Fail, c = statistical significance between CI and Null, and d = statistical significance between Null and Fail.

Variable	Abrv.	CI	Fail	Null	SS
<i>CAPE</i> [J kg^{-1}]	<i>CAPE</i>	347.33	241.92	1155.17	c, d
Mixed layer <i>CAPE</i> [J kg^{-1}]	<i>ML CAPE</i>	320.26	235.9	815.22	c, d
Most Unstable <i>CAPE</i> [J kg^{-1}]	<i>MU CAPE</i>	353.58	260.03	1175.47	c, d
Mixed layer <i>CIN</i> [J kg^{-1}]	<i>ML CIN</i>	32.72	48.52	61.19	b
Most Unstable <i>IB</i> [J kg^{-1}]	<i>MU IB</i>	-33.65	-119.19	-15.27	d
Equilibrium Level [km]	<i>EL</i>	8.36	8.33	12.36	c, d
Mixed layer <i>EL</i> [km]	<i>ML EL</i>	7.51	8.04	12.05	c, d
Most Unstable <i>EL</i> [km]	<i>MU EL</i>	8.93	8.11	12.22	c, d
Lifting Condensation Level [km]	<i>LCL</i>	2.2	2.68	2.39	d
Mixed layer <i>LCL</i> [km]	<i>ML LCL</i>	2.32	2.67	2.41	d
Most Unstable <i>LCL</i> [km]	<i>MU LCL</i>	2.16	2.58	2.34	d
Height of mixing ratio = 10 g kg^{-1} [km]	$Z_{q=10}$	1.36	1.22	2.47	c, d
Mixing ratio difference from surface to 1.5 km above <i>LFC</i> [g kg^{-1}]	<i>MRD</i>	-6.6	-5.9	-11.4	b, c, d
Mixed layer mixing ratio difference [g kg^{-1}]	<i>ML MRD</i>	-6.2	-5.7	-12.1	c, d
Most Unstable mixing ratio difference [g kg^{-1}]	<i>MU MRD</i>	-6.6	-5.9	-11.4	b, c, d
low-level (lowest 100-hPa) pot. temp. [K]	<i>LL θ</i>	303.7	304.45	309.33	c, d
Height of freezing level [km]	Z_{fm}	3.79	3.63	4.5	c, d
Free troposphere dew point depression (alt > 3.35 km) [$^{\circ}\text{C}$]	<i>FT $T - T_d$</i>	14.93	16.13	22.28	c, d
Mid-level dew point depression (600–400-hPa) [$^{\circ}\text{C}$]	<i>ML $T - T_d$</i>	12.3	12.13	22.04	c, d
Lapse rate tendency (sfc–700-hPa) [$\text{K km}^{-1} \text{hr}^{-1}$]	<i>LL LRT</i>	0.16	0.16	1.68	c
Lapse rate tendency (700–500-hPa) [$\text{K km}^{-1} \text{hr}^{-1}$]	<i>MidL LRT</i>	0.16	0.28	-0.16	c, d
Mixed layer mean ACBL lapse rate [K km^{-1}]	<i>ML ACBL</i>	-6.62	-6.93	-7.81	c
low-level (lowest 100-hPa) <i>u</i> wind [m s^{-1}]	<i>LL u</i>	-3.48	-2.94	-1.29	c
low-level (lowest 100-hPa) <i>v</i> wind [m s^{-1}]	<i>LL v</i>	-0.36	0.08	-5.11	c, d
Maximum bulk shear [m s^{-1}]	dV_{max}	20.09	18.73	15.06	c
low-level (lowest 100-hPa) <i>w</i> [m s^{-1}]	<i>LL w</i>	0.37	1.64	0.68	b
Mean <i>w</i> below <i>LFC</i> [m s^{-1}]	mean <i>w</i> (sfc to <i>LFC</i>)	0.42	1.04	0.51	b
Mean <i>w</i> above <i>LFC</i> [m s^{-1}]	<i>w</i> (above <i>LFC</i>)	0.34	0.97	0.44	b
Mixed layer mean <i>w</i> below <i>LFC</i> [m s^{-1}]	<i>ML</i> mean <i>w</i> (sfc to <i>LFC</i>)	0.47	1.07	0.43	b
Precipitable water [mm]	<i>PW</i>	24.35	20.41	26.9	d

LIST OF FIGURES

- Fig. 1.** Spatial distribution of sounding site locations during the subset of RELAMPAGO-CACTI CI missions (colored dots) within two regions (outlined in (a) blue and (b) red, respectively, in the inset) that include the Mendoza and Córdoba provinces, respectively. The main topographic features are labeled and relevant cities are denoted with black triangles. The location of the DOE-ARM site at Villa Yacanto is also annotated with a black arrow and black text. . . . 47
- Fig. 2.** Spatial (a, b) and temporal (c, d) autocorrelations for data within the (a, c) boundary layer (altitude of 0–3.35 km), and (b, d) free troposphere (altitude of 3.35–9 km). The 3.35-km (~650-hPa) division between the boundary layer and free troposphere was the deepest boundary layer height computed from all soundings used in this study. Plotted are correlograms of θ (red), mixing ratio (q ; green), zonal wind (u , blue), meridional wind (v , teal), vertical wind shear ($\frac{dV}{dZ}$; orange), and static stability ($\frac{d\theta}{dZ}$; dark red). The horizontal dashed line in all panels denotes the 0.5-autocorrelation level. Pearson correlation coefficients, representing the fit of the running mean to the raw data, is provided. . . . 48
- Fig. 3.** Examples of sounding-to-sounding variance at CI time from (a) 29 November and (b) 4 December. Sounding launch sites for each date are provided in panels (c) and (d), respectively. 49
- Fig. 4.** Observed low-level radar reflectivity for the CI/Fail event days. Radar reflectivity at various times is plotted in different colors noted in each panel, where lighter shades are 5–35 dBZ and darker shades are ≥ 35 dBZ. In all panels, terrain (m ASL) is shaded in gray. Included on each panel are the CI and Fail sounding site locations (black circles) with 30 km range rings (black), notable features (i.e., outflow boundaries, cities, or radar/site locations), terrain features, and sounding times for CI and Fail, and Null (green and blue, respectively). . . . 50
- Fig. 5.** Modeled low-level radar reflectivity for the Null event days. Simulated radar reflectivity from WRF-CAMs is plotted at 17 and 18 UTC from the CSU (blue < 35 dBZ, dark blue ≥ 35 dBZ) and UI (orange < 35 dBZ, red ≥ 35 dBZ) models. In both panels, terrain (m ASL) is shaded in gray. Included on each panel are the Null sounding site locations (black circles) with 30 km range rings (black), notable features (i.e., cities, or radar/site locations), terrain features, and sounding times (red). . . . 51
- Fig. 6.** Mean soundings representative of (a) CI (green), (b) Fail (blue), and (c) Null (red) events. The mean temperature is the solid line, mean dew point temperature is the dashed line, and mean surface-based parcel is the solid black line. The standard deviations for the mean temperature and dew point temperature are shaded in grey. The mean horizontal wind for each event type is plotted as wind barbs on the right of each panel. The horizontal dashed line in all panels denotes the approximate peak terrain height. . . . 52
- Fig. 7.** Smoothed mean atmospheric profiles of (a) Brunt–Väisälä frequency (static stability), (b) lapse rate tendency (LRT), (c) vertical wind shear, (d) dew point depression, (e) mixing ratio, and (f) w for all CI (green), Fail (blue), and Null (red) events. The horizontal dashed line in all panels denotes the approximate peak terrain height. The vertical dashed line in panels (b) and (f) denotes $LRT = 0^\circ\text{C km}^{-1} \text{hr}^{-1}$ and $w = 0 \text{ m s}^{-1}$, respectively. The standard deviations for each variable are shaded. . . . 53
- Fig. 8.** Box-and-whisker plots of (top row) IB (J kg^{-1}) and (bottom row) CIN (J kg^{-1}) for CI (green), Fail (blue), and Null events (red) assuming a (left) surface-based parcel, (middle) mixed-layer parcel, and (right) the most unstable parcel. . . . 54

Fig. 9.	Mean terrain (SDC) relative low-level winds (lowest 100-hPa) for CI (green), Fail (blue), and Null (red) events, where the north-south line is terrain parallel and west-east is terrain perpendicular. Proximity soundings to initiating convection near a secondary terrain feature to the east of the SDC, called the Sierras Chicas, are not included.	55
Fig. 10.	Visible satellite imagery from (a), (b) 21 November and (c), (d) 16 December at approximately 1738 UTC (a, c) and 1938 UTC (b, d). The prominent clear sky region is highlighted with a red circle and the horizontal convective roll region is highlighted with a yellow box. The cities of Córdoba, Rio Tercero, Rio Cuarto, and Villa Yacanto are labeled with a C, 3, 4, and Y, respectively.	56
Fig. 11.	Average convergence over the SDC peak computed from observed soundings windward/western soundings and select leeside/eastern soundings at CI time. Positive values indicate convergence, while negative values are divergence. 2 November was not included as there was no windward sounding site, and 26 November was not included as the mission was focused in the lee of the Andes. The horizontal dashed line denotes the approximate peak terrain height. The vertical dashed line denotes zero convergence. CI and Fail events are colored in green and blue tones, while Null events are colored in red tones.	57
Fig. 12.	Mean Null (red) and CI+Fail (dark green) (a), (b) soundings, (c), (d) Scorer parameter profiles, and (e), (f) zonal wind profiles west of the SDC (a, c, e) and east of the SDC (b, d, f). The horizontal dashed line in all panels denotes the approximate peak terrain height. The vertical dashed line in panels (e) and (f) denote $u = 0 \text{ m s}^{-1}$. The standard deviations are shaded. Due to relatively few soundings for the Null category, the standard deviation for the Scorer parameter (panels c and d) do not include highly erroneous outlier data greater than $40 \times 10^{-5} \text{ m}^{-2}$ (less than 2% of the data).	58
Fig. 13.	Box plots of F_n for CI+Fail (dark green) and Null (red) soundings west and east of the SDC. Also provided are the total number of soundings (N) in each group.	59

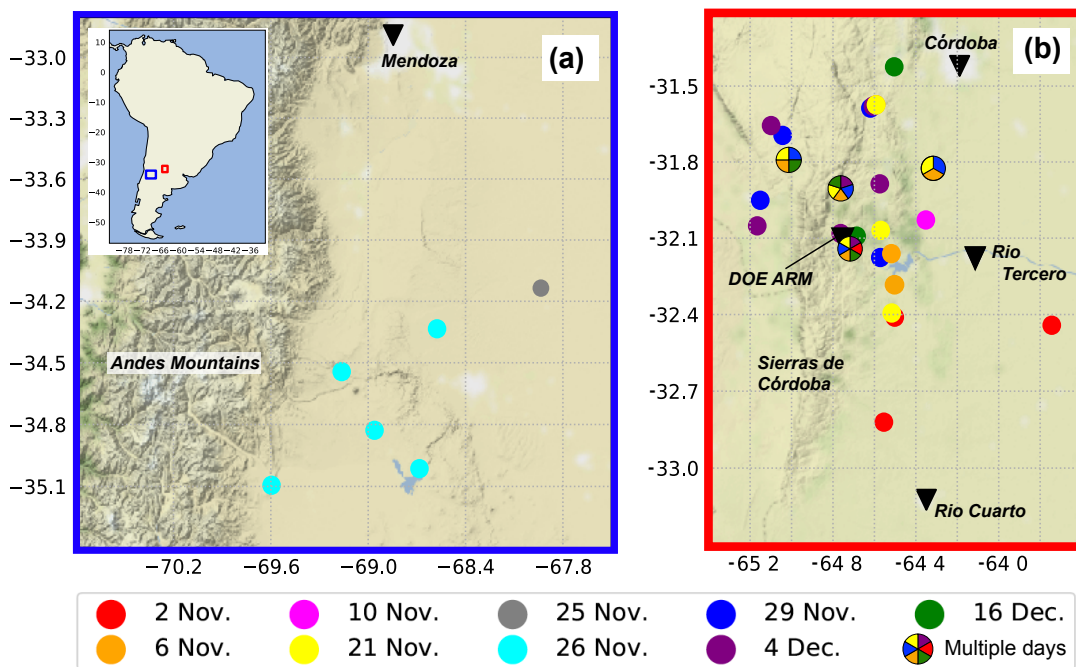


FIG. 1. Spatial distribution of sounding site locations during the subset of RELAMPAGO-CACTI CI missions (colored dots) within two regions (outlined in (a) blue and (b) red, respectively, in the inset) that include the Mendoza and Córdoba provinces, respectively. The main topographic features are labeled and relevant cities are denoted with black triangles. The location of the DOE-ARM site at Villa Yacanto is also annotated with a black arrow and black text.

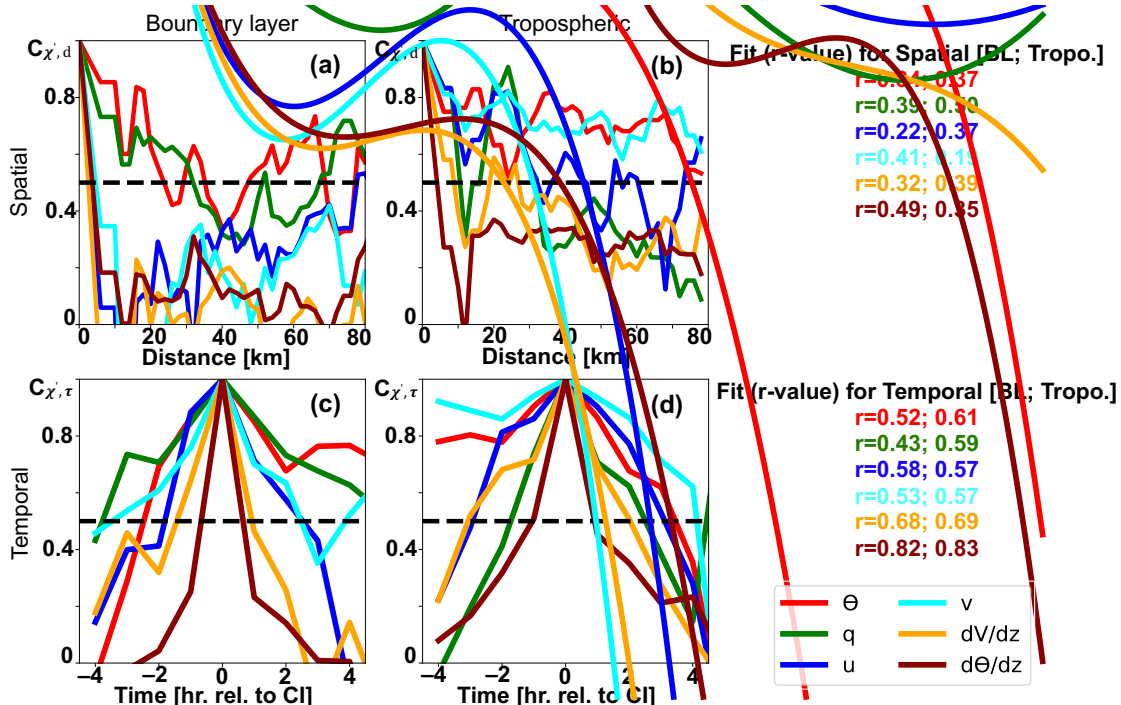


FIG. 2. Spatial (a, b) and temporal (c, d) autocorrelations for data within the (a, c) boundary layer (altitude of 0–3.35 km), and (b, d) free troposphere (altitude of 3.35–9 km). The 3.35-km (~ 650 -hPa) division between the boundary layer and free troposphere was the deepest boundary layer height computed from all soundings used in this study. Plotted are correlograms of θ (red), mixing ratio (q ; green), zonal wind (u , blue), meridional wind (v , teal), vertical wind shear ($\frac{dV}{dz}$ orange), and static stability ($\frac{d\theta}{dz}$; dark red). The horizontal dashed line in all panels denotes the 0.5-autocorrelation level. Pearson correlation coefficients, representing the fit of the running mean to the raw data, is provided.

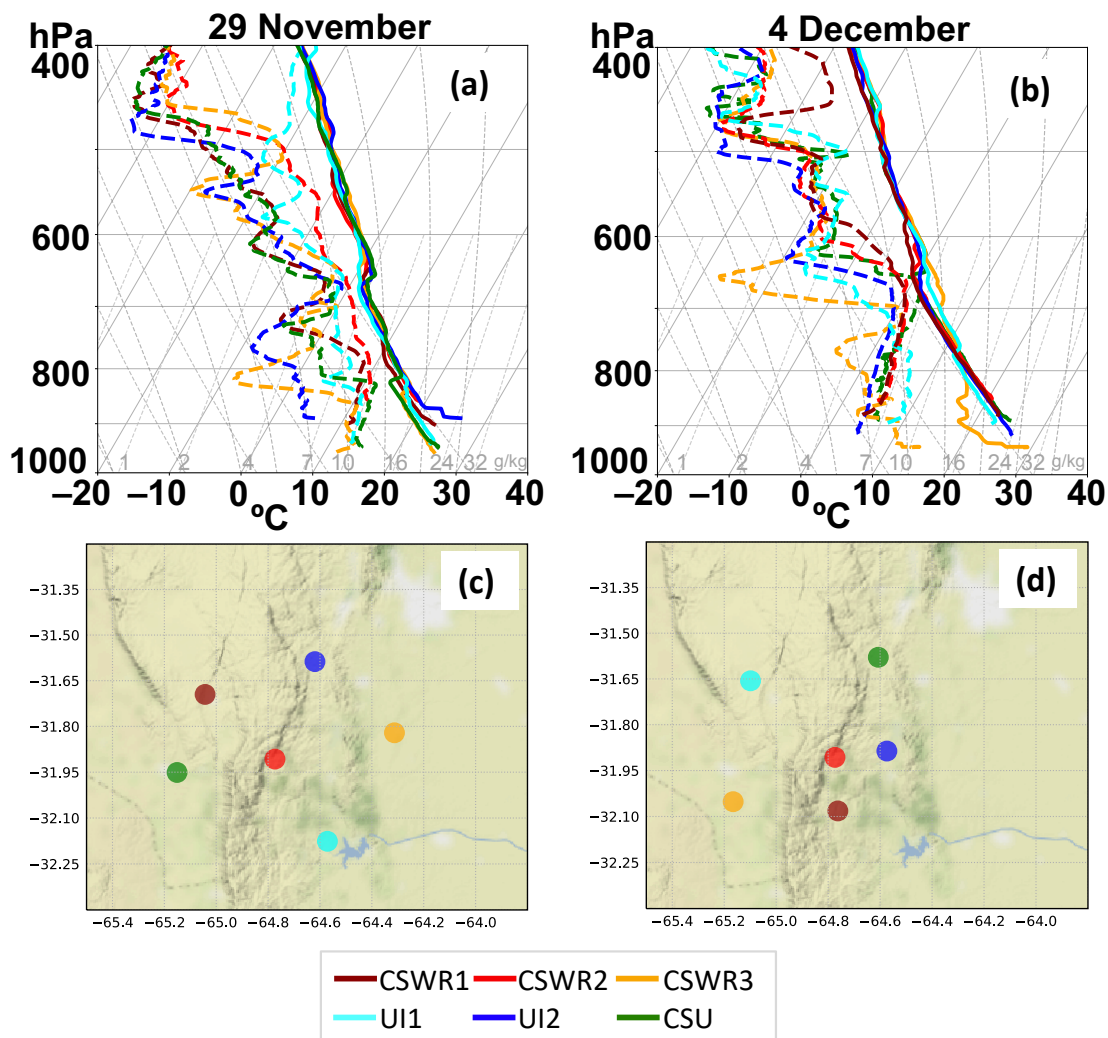


FIG. 3. Examples of sounding-to-sounding variance at CI time from (a) 29 November and (b) 4 December. Sounding launch sites for each date are provided in panels (c) and (d), respectively.

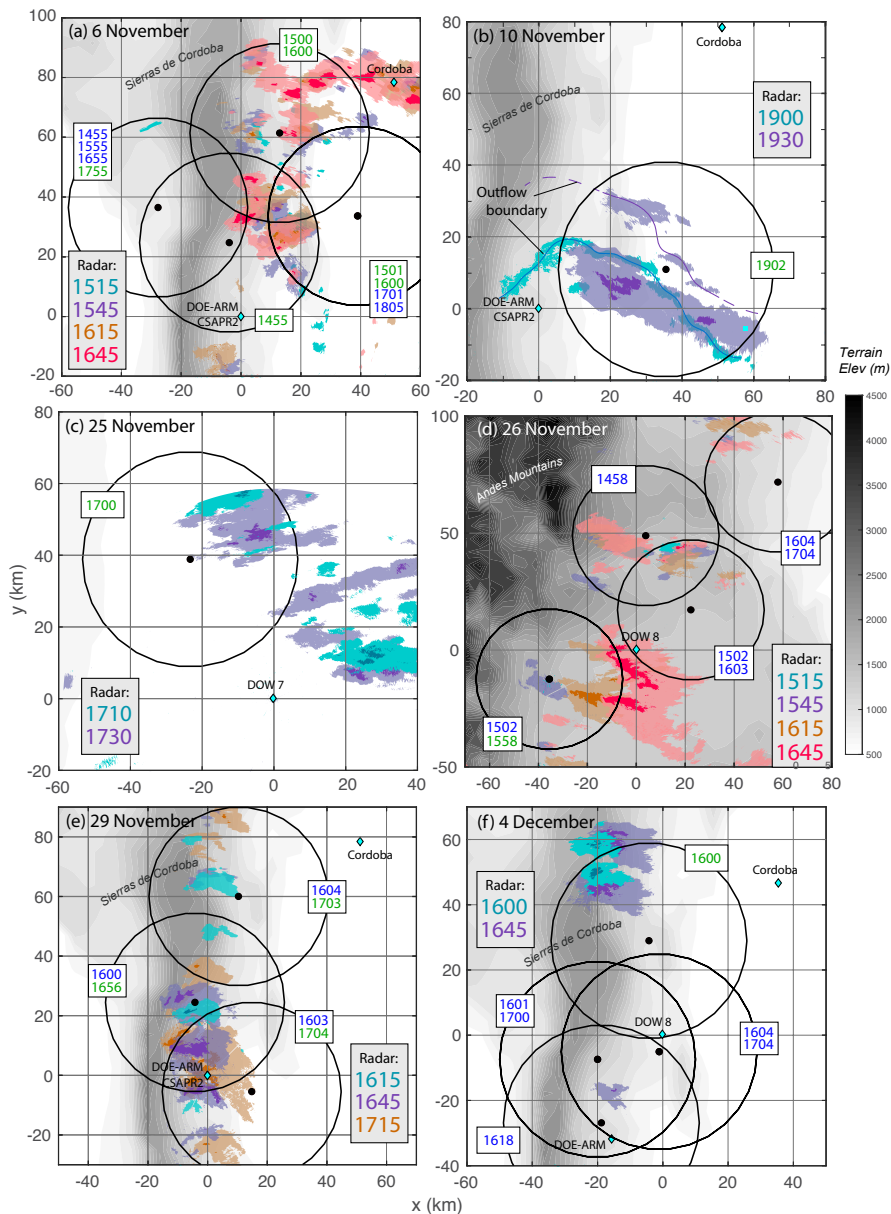


FIG. 4. Observed low-level radar reflectivity for the CI/Fail event days. Radar reflectivity at various times is plotted in different colors noted in each panel, where lighter shades are 5–35 dBZ and darker shades are ≥ 35 dBZ. In all panels, terrain (m ASL) is shaded in gray. Included on each panel are the CI and Fail sounding site locations (black circles) with 30 km range rings (black), notable features (i.e., outflow boundaries, cities, or radar/site locations), terrain features, and sounding times for CI and Fail, and Null (green and blue, respectively).

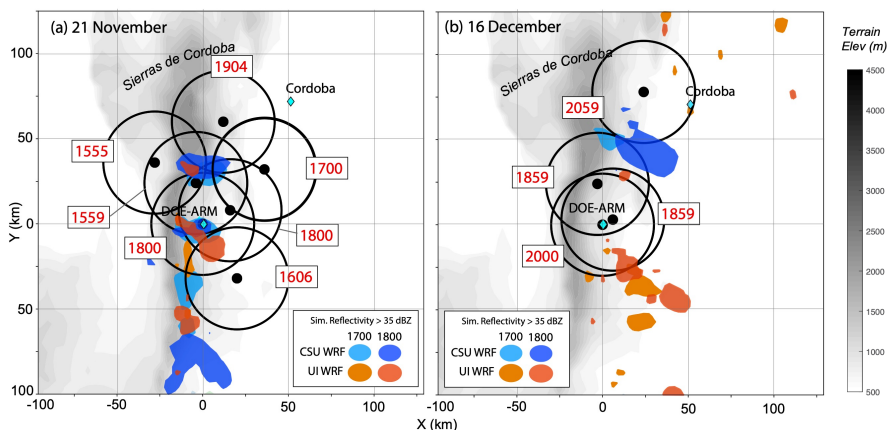


FIG. 5. Modeled low-level radar reflectivity for the Null event days. Simulated radar reflectivity from WRF-CAMs is plotted at 17 and 18 UTC from the CSU (blue < 35 dBZ, dark blue ≥ 35 dBZ) and UI (orange < 35 dBZ, red ≥ 35 dBZ) models. In both panels, terrain (m ASL) is shaded in gray. Included on each panel are the Null sounding site locations (black circles) with 30 km range rings (black), notable features (i.e., cities, or radar/site locations), terrain features, and sounding times (red).

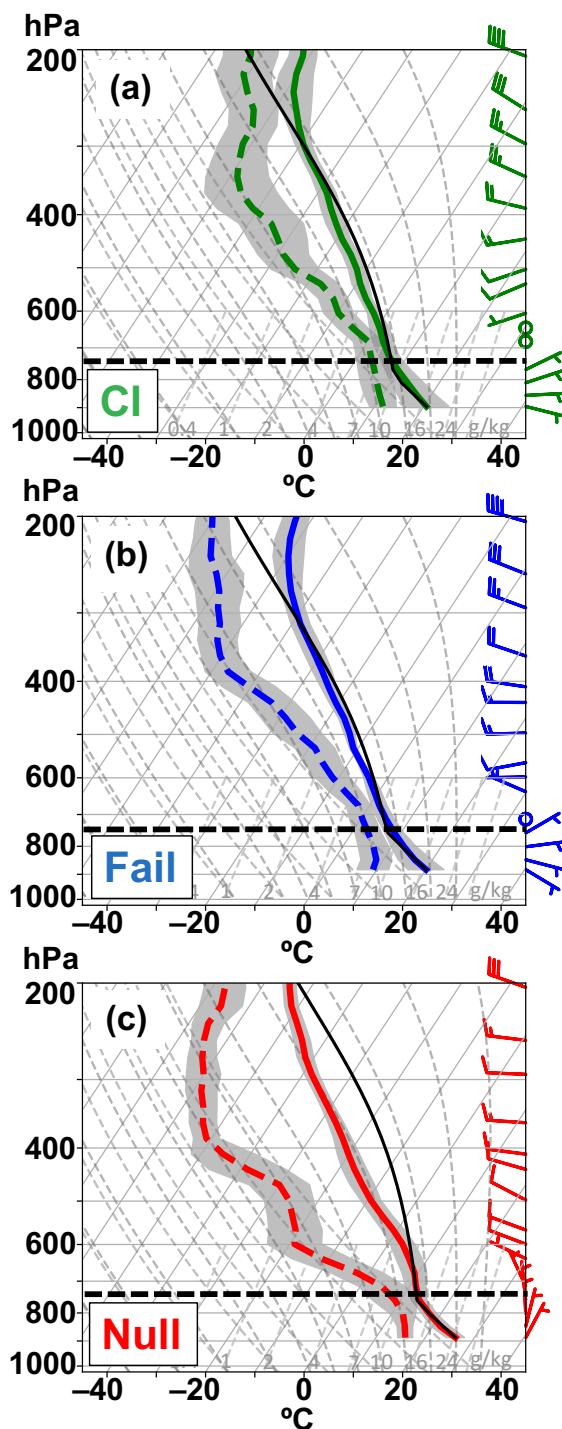


FIG. 6. Mean soundings representative of (a) CI (green), (b) Fail (blue), and (c) Null (red) events. The mean temperature is the solid line, mean dew point temperature is the dashed line, and mean surface-based parcel is the solid black line. The standard deviations for the mean temperature and dew point temperature are shaded in grey. The mean horizontal wind for each event type is plotted as wind barbs on the right of each panel. The horizontal dashed line in all panels denotes the approximate peak terrain height.

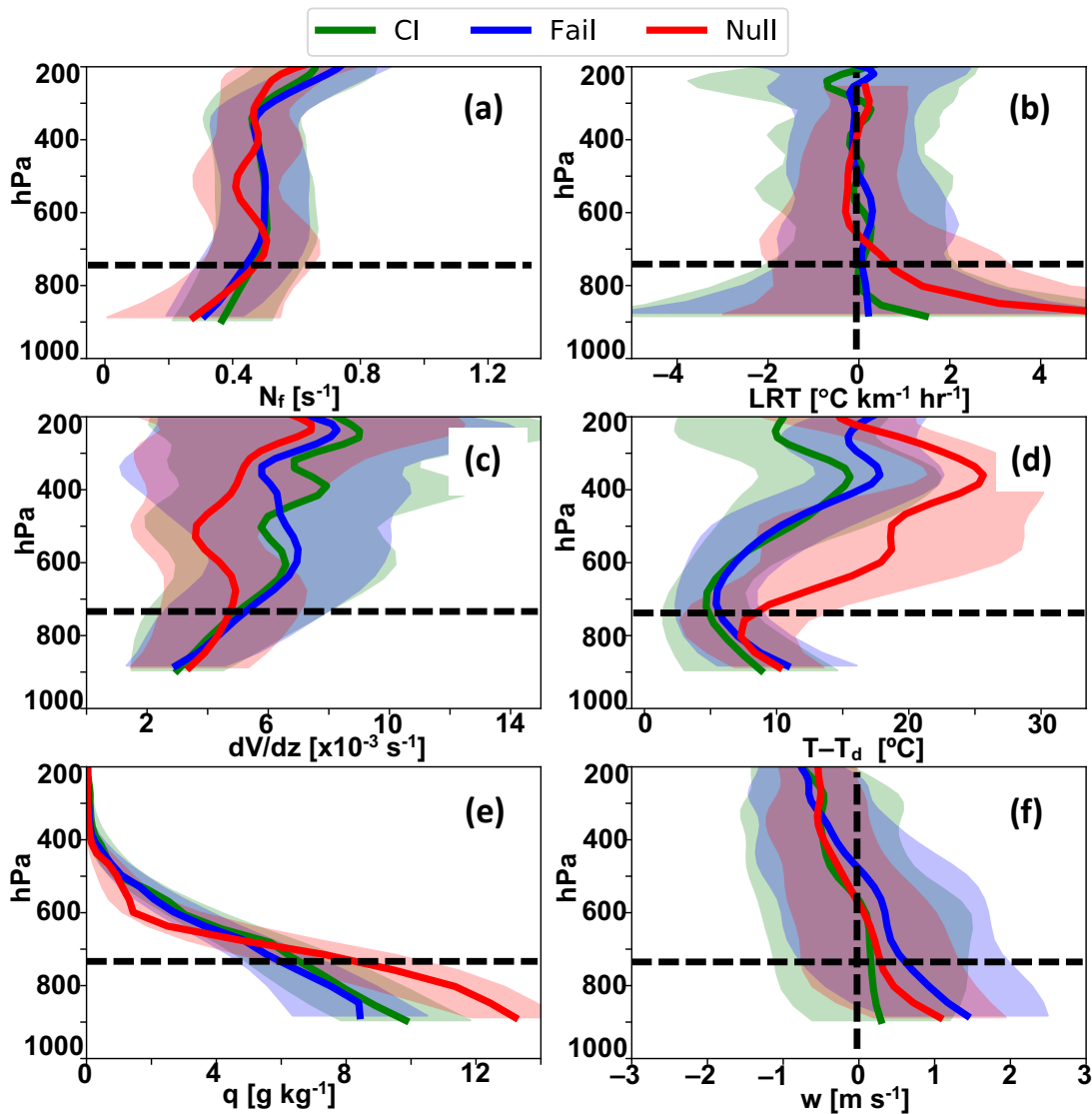


FIG. 7. Smoothed mean atmospheric profiles of (a) Brunt–Väisälä frequency (static stability), (b) lapse rate tendency (LRT), (c) vertical wind shear, (d) dew point depression, (e) mixing ratio, and (f) w for all CI (green), Fail (blue), and Null (red) events. The horizontal dashed line in all panels denotes the approximate peak terrain height. The vertical dashed line in panels (b) and (f) denotes $LRT = 0^\circ\text{C km}^{-1}\text{ hr}^{-1}$ and $w = 0\text{ m s}^{-1}$, respectively. The standard deviations for each variable are shaded.

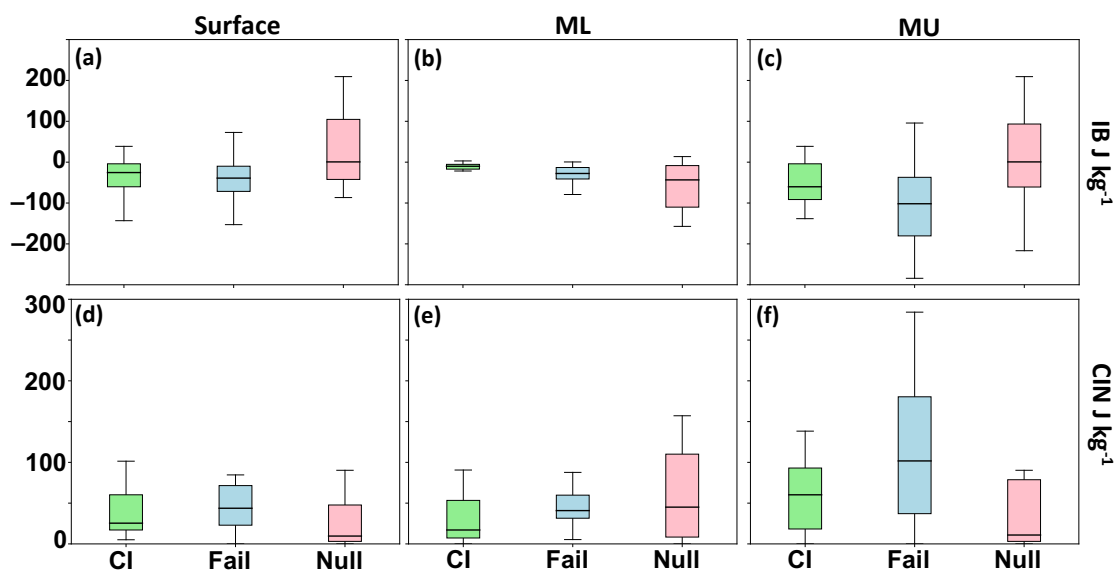


FIG. 8. Box-and-whisker plots of (top row) IB ($J kg^{-1}$) and (bottom row) CIN ($J kg^{-1}$) for CI (green), Fail (blue), and Null events (red) assuming a (left) surface-based parcel, (middle) mixed-layer parcel, and (right) the most unstable parcel.

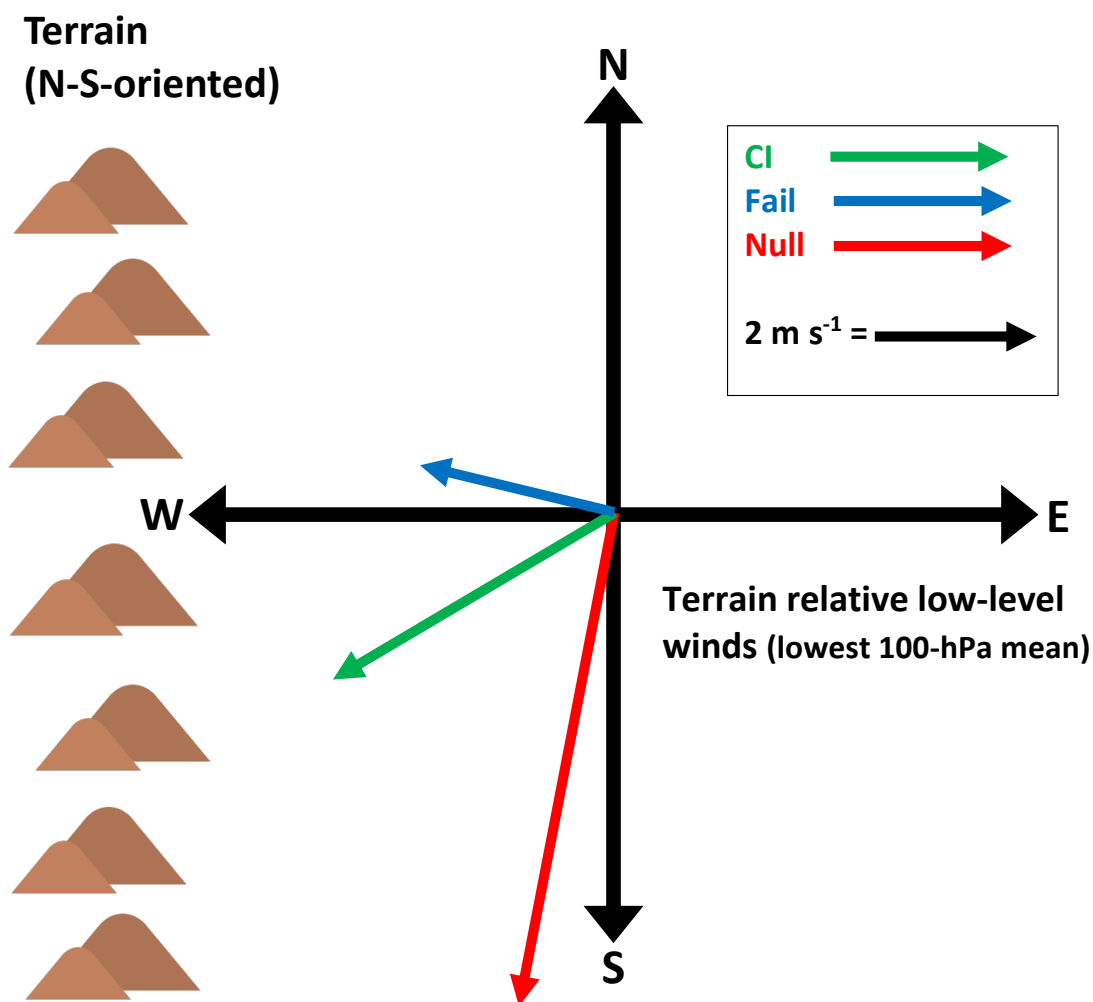


FIG. 9. Mean terrain (SDC) relative low-level winds (lowest 100-hPa) for CI (green), Fail (blue), and Null (red) events, where the north-south line is terrain parallel and west-east is terrain perpendicular. Proximity soundings to initiating convection near a secondary terrain feature to the east of the SDC, called the Sierras Chicas, are not included.

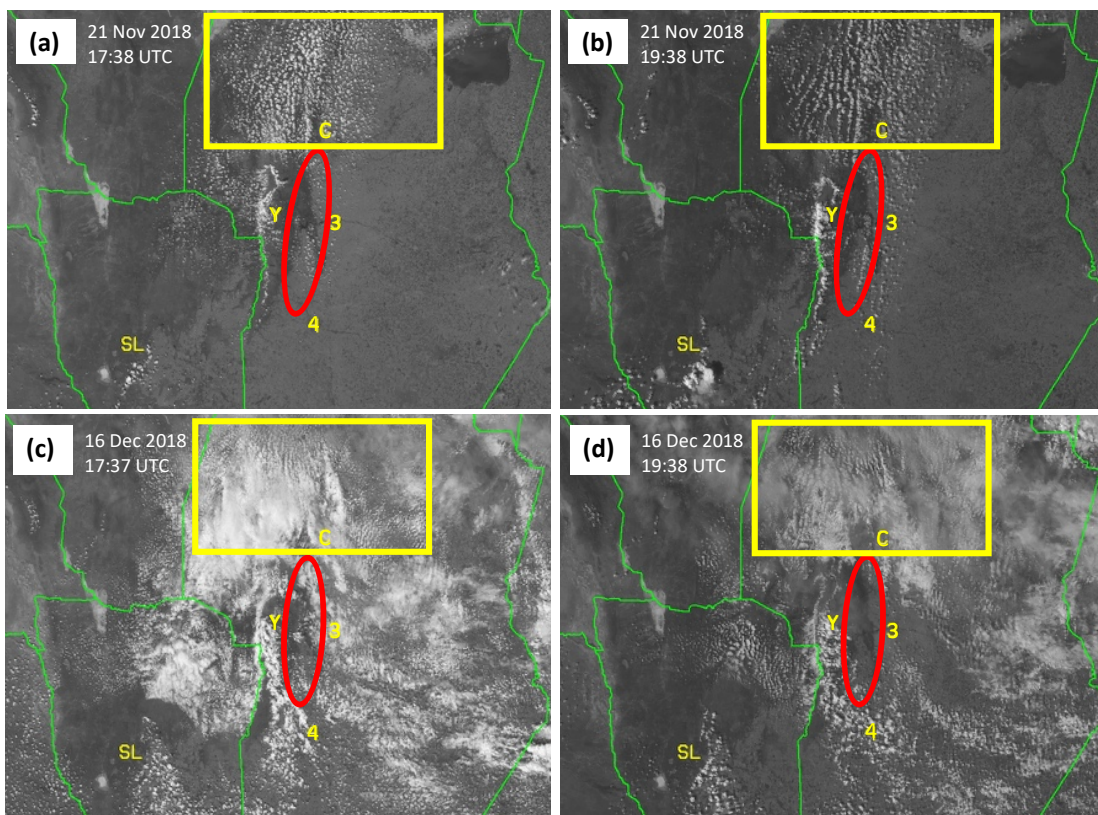


FIG. 10. Visible satellite imagery from (a), (b) 21 November and (c), (d) 16 December at approximately 1738 UTC (a, c) and 1938 UTC (b, d). The prominent clear sky region is highlighted with a red circle and the horizontal convective roll region is highlighted with a yellow box. The cities of Córdoba, Rio Tercero, Rio Cuarto, and Villa Yacanto are labeled with a C, 3, 4, and Y, respectively.

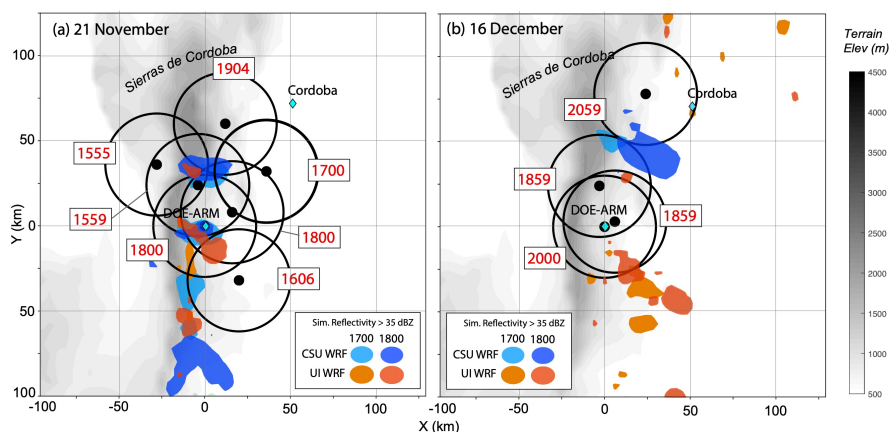


FIG. 5. Modeled low-level radar reflectivity for the Null event days. Simulated radar reflectivity from WRF-CAMs is plotted at 17 and 18 UTC from the CSU (blue < 35 dBZ, dark blue ≥ 35 dBZ) and UI (orange < 35 dBZ, red ≥ 35 dBZ) models. In both panels, terrain (m ASL) is shaded in gray. Included on each panel are the Null sounding site locations (black circles) with 30 km range rings (black), notable features (i.e., cities, or radar/site locations), terrain features, and sounding times (red).

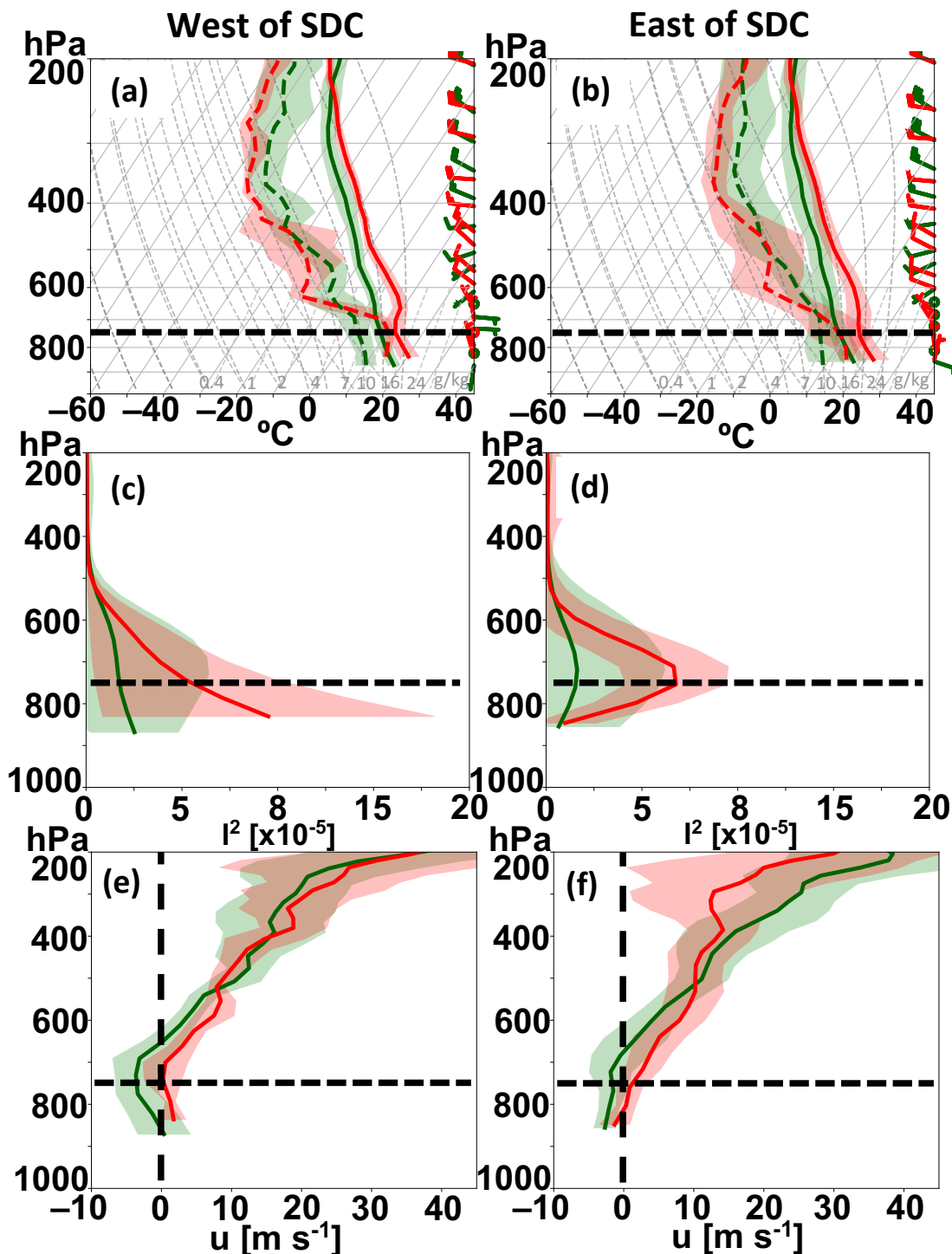


FIG. 12. Mean Null (red) and CI+Fail (dark green) (a), (b) soundings, (c), (d) Scorer parameter profiles, and (e), (f) zonal wind profiles west of the SDC (a, c, e) and east of the SDC (b, d, f). The horizontal dashed line in all panels denotes the approximate peak terrain height. The vertical dashed line in panels (e) and (f) denote $u = 0 \text{ m s}^{-1}$. The standard deviations are shaded. Due to relatively few soundings for the Null category, the standard deviation for the Scorer parameter (panels c and d) do not include highly erroneous outlier data greater than $40 \times 10^{-5} \text{ m}^{-2}$ (less than 2% of the data).

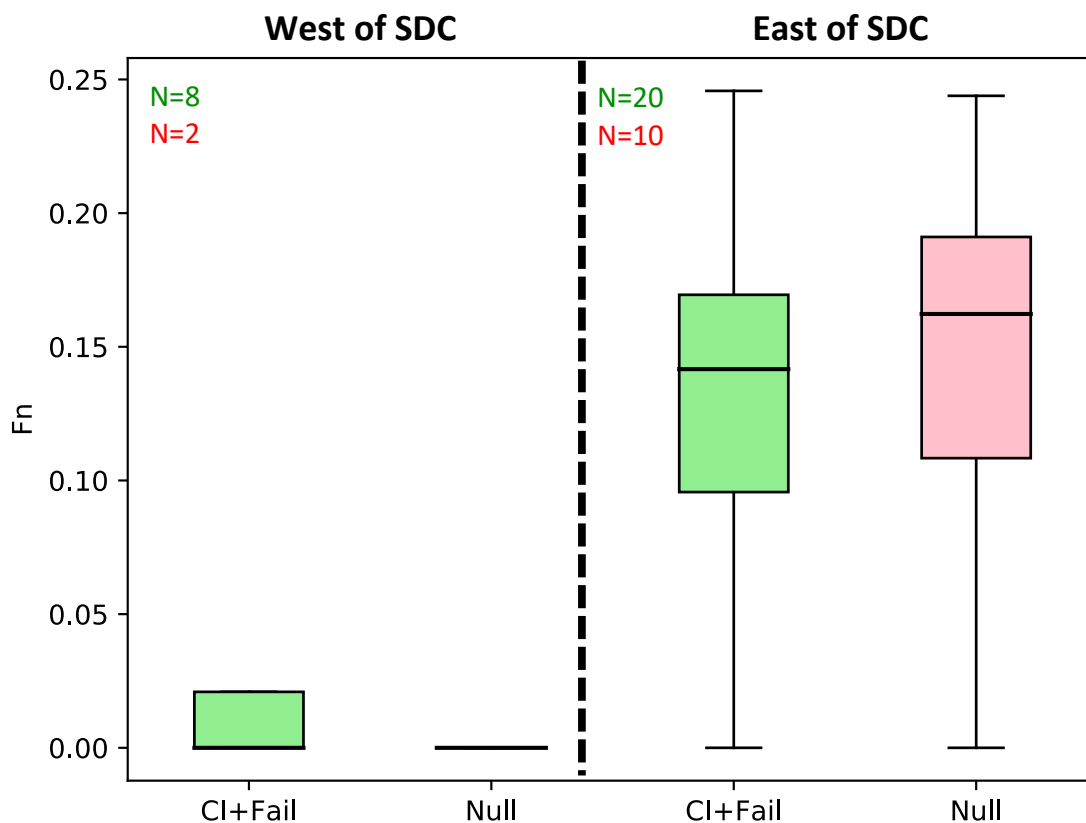


FIG. 13. Box plots of F_n for CI+Fail (dark green) and Null (red) soundings west and east of the SDC. Also provided are the total number of soundings (N) in each group.